Structure. Author manuscript; available in PMC 2024 April 06.

E6AP AZUL interaction with UBQLN1/2 in cells, condensates, and an AlphaFold-NMR integrated structure

Gwen R. Buel[1], **Xiang Chen**[1], **Wazo Myint**[2], **Olumide Kayode**[1], **Varvara Folimonova**[1], **Anthony Cruz**[1], **Katarzyna A Skorupka**[2], **Hiroshi Matsuo**[2], **Kylie J. Walters**[1,3,*]

[1]Protein Processing Section, Center for Structural Biology, Center for Cancer Research, National Cancer Institute, National Institutes of Health, Frederick, MD 21702, USA.

[2]Cancer Innovation Laboratory, Frederick National Laboratory for Cancer Research, Frederick, MD 21702, USA

[3]Lead Contact

Summary

The E3 ligase E6AP/UBE3A has a dedicated binding site in the 26S proteasome provided by the RAZUL domain of substrate receptor hRpn10/S5a/PSMD4. Guided by RAZUL sequence similarity, we test and demonstrate here that the E6AP AZUL binds transiently to the UBA of proteasomal shuttle factor UBQLN1/2. Despite a weak binding affinity, E6AP AZUL is recruited to UBQLN2 biomolecular condensates *in vitro* and E6AP interacts with UBQLN1/2 *in cellulo*. Steady-state and transfer NOE experiments indicate direct interaction of AZUL with UBQLN1 UBA. Intermolecular contacts identified by NOESY data were combined with AlphaFold2-Multimer predictions to yield an AZUL:UBA model structure. We also identify an oligomerization domain directly adjacent to UBQLN1/2 UBA (UBA-adjacent, UBAA) that is α-helical and allosterically reconfigured by AZUL binding to UBA. These data lead to a model of E6AP recruitment to UBQLN1/2 by AZUL:UBA interaction and provide fundamental information on binding requirements for interactions in condensates and cells.

Graphical Abstract

---

[*] Corresponce: kylie.walters@nih.gov.

Author Contributions

G.R.B., W.M., and K.J.W. conceived of and designed the experiments. G.R.B., X.C., and O.K. performed experiments and data analyses. W.M. performed CPMG R_2 relaxation-dispersion experiments and analyses. V.F. expressed and purified UBQLN1 UBA (541-589). A.C. assisted with sample preparation. K.A.S. assisted with SEC-MALS technical issues and data interpretation. G.R.B., H.M., and K.J.W interpreted results. G.R.B. and K.J.W. wrote the manuscript with input from all authors.

Declaration of interests

The corresponding author (K.J.W.) is a member of the *Structure* Advisory Board.

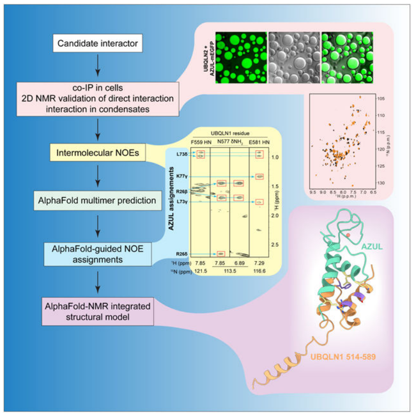

eTOC blurb

Buel et al. discover the E3 ligase E6AP AZUL to interact with the UBA of the UBQLN family of proteasome shuttle factors and a helical UBQLN UBA-adjacent domain that oligomerizes and allosterically senses AZUL binding to UBA. They further solve the AZUL:UBA structure by integrating AlphaFold2-Multimer with NMR NOESY data.

Keywords

E6AP; UBE3A; UBQLN1/2; proteasome; E3 ligase; AlphaFold; biomolecular condensates

Introduction

The ubiquitin-proteasome pathway removes proteins that are misfolded or no longer needed in cells[1]. Its substrates are marked for degradation by post-translational modification with ubiquitin[2]. Ubiquitination begins with ATP-dependent charging of the ubiquitin C-terminus by an E1 activating enzyme for subsequent thioester transfer to an E2 conjugating enzyme. An E3 ligase next acts as either a scaffold to facilitate direct transfer of ubiquitin from the E2 to a substrate or as an intermediary receptor by first accepting ubiquitin from the E2 before passing it to the substrate. The E3 ligase E6AP/UBE3A belongs to the latter class of E3s and is the namesake of this protein family called HECT (homologous to the E6AP carboxyl terminus) E3s. E6AP is infamous for its roles in human disease; human papilloma viral (HPV) oncoprotein E6 binds E6AP and directs its activity towards tumor suppressor p53, contributing to cervical cancer[3–5]. E6AP can also promote metastatic prostate cancer[6,7] and is implicated in neurological disorders, with loss-of-function mutations linked to Angelman syndrome[8–10] and elevated gene dosage with autism spectrum disorders[11].

An AZUL (amino-terminal z*inc*-binding *domain* of ubiquitin E3a ligase) domain[12] in E6AP binds to an intrinsically disordered region in the proteasome ubiquitin receptor protein hRpn10/S5a/PSMD4, so-named RAZUL (Rpn10 AZUL-binding domain)[13]. Binding to E6AP AZUL causes RAZUL to form two α-helices that interact with two AZUL α-helices to form a 4-helix bundle and loss of this interaction leads to loss of proteasome-associated E6AP[13]. E6AP has three isoforms with distinct localization to the nucleus or cytosol in neurons[14,15]. Nuclear E6AP localization is contingent on AZUL-mediated interaction with hRpn10, and E6AP mislocalization causes physiological defects[15]. Other E3 ligases associate with the proteasome[13,16–19] but without known binding mechanisms.

Nuclear E6AP and proteasomes co-localize to biomolecular condensates that are induced by hyperosmotic stress or nutrient deprivation and require RAD23B and ubiquitinated proteins[20,21]. RAD23B and closely related Rad23A belong to a larger family of ‘shuttle factor’ proteins, so-named by their ability to deliver ubiquitinated proteins to the proteasome, that also includes DDI1/2 and UBQLN proteins (UBQLN1–4 and UBQLNL)[22]. RAD23B and UBQLN1/2 are found associated with proteasomes purified from cells[18,23,24] and can stimulate proteasomal ATP hydrolysis and proteolysis[25] through a mechanism that has not yet been elucidated. UBQLN proteins can recruit an E3 ligase of unknown identity to ubiquitinate bound substrates through an interaction involving the UBA domain[26], which is known to bind ubiquitin[27–29] and contribute to interaction with the proteasome[30].

The UBA in UBQLN2 contributes to the ability of UBQLN2 to form biomolecular condensates[31,32] and RAD23B’s two UBA domains similarly drive formation of nuclear condensates containing proteasomes[20]. K48-linked ubiquitin chains appear to drive formation of RAD23B condensates[20] and K48- or K63-linked ubiquitin chains slightly or strongly promote UBQLN2 condensate formation, respectively[33].

Here, we find that a C-terminal region of UBQLN1/2 that includes its UBA domain has sequence similarity to the hRpn10 RAZUL, with conservation of amino acids involved in binding to E6AP. We use NMR (nuclear magnetic resonance) spectroscopy to test and confirm that the E6AP AZUL binds to the UBQLN1 UBA region. We find evidence of this interaction in cells and observe association of the E6AP AZUL with UBQLN2 condensates in an *in vitro* assay. By integrating NMR and biophysical data with AlphaFold2-Multimer, we generate a structural model of the UBA:AZUL complex and of a UBA adjacent (UBAA) domain that is helical and self-associates. Together, our data suggest that the E6AP AZUL binds to the UBQLN1/2 UBA and this interaction allosterically impacts UBQLN UBAA self-association.

Results

E6AP binds to UBQLN1 and UBQLN2 in cells

Following our discovery that E6AP binds to hRpn10 RAZUL through its AZUL domain[13], we searched for proteins with sequence similarity to the RAZUL domain to identify other potential binders of E6AP AZUL. This approach identified a region with 34.1% and 28.6% identity (51.2% and 50% similarity) to RAZUL within UBQLN1 and UBQLN2 respectively (Figure 1A). These two isoforms are the most closely related of the UBQLN proteins (Figure S1A), with 88% sequence identity in the identified region (Figure 1A). The other UBQLN proteins were not identified in our search despite homology in this region for UBQLN3 and UBQLN4 (Figure S1B). The RAZUL helices ($\alpha 1$ and $\alpha 2$) align to a UBQLN1/2 region N-terminally adjacent to the UBA domain and to the linker between the UBA helices $\alpha 1$ and $\alpha 2$ (Figure 1A), with multiple amino acids involved in binding to AZUL conserved[13].

To test whether E6AP interacts with UBQLN1/2 in cells, we performed immunoprecipitation experiments on cells treated with the crosslinker dithiobis(succinimidyl propionate) (DSP), an approach that allows co-immunoprecipitation of weak or transient protein complexes. One confounding issue that we anticipated for these experiments is that E6AP and the UBQLN proteins each bind to hRpn10 (Figure 1B); E6AP interacts with RAZUL[13] and UBQLN UBL binds hRpn10 UIMs[34], predominantly through UIM1[35]. To test whether E6AP interacts with UBQLN1/2 in an hRpn10-independent manner, we used a CRISPR-edited HCT116 cell line with RAZUL deleted (ΔRAZUL cells) (Figure 1C)[13]. E6AP protein levels are reduced in this cell line (Figure 1D, lane 1 compared to lane 4), as demonstrated previously[13] by an unknown mechanism. While hRpn10 co-immunoprecipitates with E6AP in the parental cell line (RAZUL WT) (Figure 1D, lane 3), it cannot bind to E6AP when its RAZUL domain is deleted (Figure 1D, lane 6). E6AP co-immunoprecipitated with both UBQLN1 and UBQLN2 in the parental HCT116 cells (Figure 1E, lanes 3–4) as well as in the ΔRAZUL cells (Figure 1E, lanes 7–8), indicating that E6AP and UBQLN1/2 can interact independently of hRpn10 (modeled in Figure 1C). UBQLN1/2 also retained interaction with hRpn10 lacking the RAZUL domain (Figure 1E, lanes 7–8), as expected (Figure 1C).

E6AP AZUL helices interact with UBQLN1

To test whether the E6AP AZUL directly interacts with the identified C-terminal region of UBQLN1/2, we used 2D NMR spectroscopy. We produced unlabeled UBQLN1 (514–589) with F547 substituted with tyrosine (514–589, F547Y) to enable quantitation of the protein concentration by absorbance at 280 nm. We compared 2D ^{15}N-HSQC spectra of 0.05 mM ^{15}N-E6AP AZUL before and after UBQLN1 (514–589, F547Y) addition (Figure S2A). AZUL amide signals shifted progressively with increasing concentrations of UBQLN1, allowing the signals to be followed from their unbound positions in the spectrum to their UBQLN1-bound positions (Figure 2A for I70 and L73). To identify the specific AZUL region that interacts with UBQLN1, we quantified the signal shifting for each backbone amide signal at 1:8 molar ratio of AZUL:UBQLN1 and plotted the values according to residue number (Figure 2B) by using chemical shift assignments from our previous study[13]. This analysis revealed the largest effects for residues in the two helices of the E6AP AZUL (Figure 2C), the same region used to bind hRpn10 RAZUL (Figure 2D).

E6AP AZUL is recruited to UBQLN2 condensates in vitro

UBQLN2 forms biomolecular condensates in cells and in isolation[31,36], and there is some evidence that UBQLN1 may do so as well[37]. We therefore tested whether E6AP AZUL associates with UBQLN biomolecular condensates as an assay for interaction. We purified UBQLN1 and UBQLN2 full-length constructs and attempted to induce formation of condensates by incubating each sample separately at 37°C in the presence of 200 mM NaCl as done previously for UBQLN2[31]. Under these conditions, we observed condensates of UBQLN2 (Figure 2E); however, no condensate formation was observed for UBQLN1 (not shown). These results suggest that UBQLN1 cannot form condensates in isolation under the same conditions as UBQLN2, and perhaps different stimuli are required for UBQLN1 condensate formation.

To test whether E6AP AZUL is recruited to UBQLN2 condensates, we considered various options for fluorescent tagging. Due to the presence of cysteine residues and their coordination of zinc as required for AZUL structural integrity[12,38], we avoided chemical synthesis approaches. Instead, we chose a form of EGFP to tag AZUL, since GFP-tagging had been used previously to show association of RNA polymerase II with FUS low-complexity domain condensates[39] and a control experiment with EGFP alone added to UBQLN2 condensates indicated its exclusion (Figure 2F). EGFP was fused to the C-terminus of E6AP AZUL, with EGFP containing the A206K mutation (mEGFP) to decrease its propensity for dimerization[40] and thereby avoid effects caused by unintended EGFP self-association. When we mixed AZUL-mEGFP with UBQLN2 and induced condensate formation, we found the EGFP signal to localize to the UBQLN2 condensates (Figure 2G, top panels), indicating that E6AP AZUL associates with UBQLN2 condensates. As expected, condensate formation is not observed for AZUL-mEGFP in the absence of UBQLN2 (Figure 2G, bottom panels).

The UBA-adjacent (UBAA) region of UBQLN1 is helical and structurally independent of UBA

The structure of the UBQLN UBA domain encompassing amino acids Q541 to S589 had been solved[41], however, there was no structural information available for the region N-terminally adjacent to the UBA. To gain insight into the structure of this region, we used AlphaFold2[42,43] to generate a model of the UBQLN1 C-terminal region under study, spanning 514–589. The resulting structure correctly predicted the three helices of UBA[41] and additionally predicted a region in spanning Q524-A534 to be helical; we name this region UBA-adjacent (UBAA, Figure 3A). To experimentally assess the helicity of UBAA, we assigned chemical shift values to the amide H, ^{H}N, C’, Cα, and Cβ atoms of UBQLN1 (514–586), as described in Methods, and inputted this information into the secondary structure prediction software TALOS+[44]. The UBA domain helices were identified as helical, as was the region corresponding to F526-A532 (Figure 3B), consistent with AlphaFold2 (Figure 3A). Moreover, in a ^{15}N-edited nuclear Overhauser effect Spectroscopy (NOESY) experiment acquired on 0.6 mM ^{15}N-labeled UBQLN1 (514–589, F547Y), we observed interactions between amide hydrogen atoms that defined the region spanning Q524-A534 as being helical (Figure S3A). Of note, no interactions were detected between UBA and UBAA, suggesting that these two regions do not interact with each other, in agreement with the AlphaFold2-predicted structure (Figure 3A).

As an independent assessment of whether the UBQLN1 UBA and UBAA domains interact, we measured the dynamic behavior of ^{15}N-UBQLN1 (514–589, F547Y) by recording heteronuclear NOE enhancements (hetNOE). The hetNOE values in UBAA were lower than those in the UBA region (Figure 3C, left panel), with measurements at two different concentrations in agreement (600 and 50 μM). This finding indicates that these two UBQLN1 regions have distinct dynamical features consistent with UBAA and UBA not interacting, and moreover, that UBAA undergoes faster internal motion than the UBA domain.

Based on our initial hypothesis that AZUL binds to UBAA together with part of UBA (Figure 1A), we next tested whether AZUL binding brings these two regions together. To interrogate this model, we purified ^{2}H-^{15}N-UBQLN1 (514–589, F547Y) and mixed it with 2-fold molar excess unlabeled AZUL. The hetNOE values acquired on this sample (Figure 3C, right panel) were similar to the values of UBQLN1 without AZUL, indicating that these domains remain separate in the presence of AZUL.

In our studies of E6AP and hRpn10, we found E6AP AZUL to induce helicity in hRpn10 RAZUL[13]. To test whether AZUL similarly induces helicity in the UBQLN1 UBAA, we evaluated the circular dichroism (CD) trace of an equimolar mixture of UBQLN1 and AZUL compared to the isolated proteins. A nearly identical profile was recorded for the mixed sample compared to the theoretical sum of values obtained from unmixed UBQLN1 and AZUL, indicating that AZUL does not affect the helicity of UBQLN1 UBAA or UBA (Figure S3B).

During our NMR experiments with UBQLN1 (514–589, F547Y), we used varying protein concentrations and found that the UBAA signals varied slightly. These differences are apparent by comparing ^{15}N-HSQC spectra recorded on ^{15}N-UBQLN1 (514–589, F547Y) at 50 μM and 600 μM concentration (Figure 3D). Plotting the quantified backbone amide atom shifting across the UBQLN1 sequence reveals a cluster of concentration-dependent shifts in the region spanning UBAA (H522-N357, Figure 3E). Consistent with a model of self-association, examination of the UBAA helix from the AlphaFold2-predicted structure revealed it to be amphipathic, with a high density of glutamine residues comprising the polar side and a hydrophobic surface that could potentially drive oligomerization (Figure 3F).

UBAA undergoes concentration-dependent oligomerization

To investigate further the dynamics of individual amino acid residues in UBQLN1 at the picosecond to nanosecond time scale, we performed NMR longitudinal (R_1) and transverse (R_2) relaxation experiments at high (600 μM) and low (50 μM) concentrations of ^{15}N-UBQLN1. The R_1 rates consistently indicated slightly lower values at 50 μM compared to 600 μM concentration (Figure 4A), a trend also observed for UBA R_2 rates (Figure 4A). In UBAA however, the region spanning I526 – G535 displayed noticeably elevated R_2 values in the higher concentration sample (Figure 4A), suggesting a more ordered conformation and/or chemical exchange in this region. This finding is supportive of self-association in the UBAA and consistent with a previous study in which regions within UBQLN2 (450–624) thought to be responsible for self-association were found to undergo concentration-dependent signal shifting and/or R_2 rates sensitive to dimerization[31].

We also measured R_1 and R_2 relaxation rates for the same sample used in Fig 3C containing E6AP AZUL (Figure 4B). We found the R_2 rates were enhanced throughout the length of the protein compared to the sample without AZUL, as expected for deuterated samples. As in the more concentrated sample for free UBQLN1, many UBAA residues showed increased R_2 rates compared to UBA residues. In particular, I526 and A534 were elevated in the high-concentration samples, with or without AZUL present (Figure 4A–B, bottom panels). Q527 was elevated in the high-concentration sample without AZUL, whereas L530 was elevated in the sample containing AZUL (Figure 4A versus B). R_2 values were decreased for the region between the UBAA and UBA domains in the high-concentration sample and with AZUL present, indicating it to be more flexible than the two domains under these conditions (Figure 4A–B bottom left and right panels and Fig 4C). The R_1 rates were relatively similar throughout the length of the protein for the two concentrations of UBQLN1 (Figure 4A top panel, and Fig 4C); however, addition of AZUL reduced R_1 values in UBA (Figure 4B top panel and Fig 4C), indicative of a larger molecular mass caused by AZUL binding.

To test further whether the concentration-dependent effects observed for UBAA are caused by self-association, we performed size exclusion chromatography coupled to multi-angle light scattering (SEC-MALS). Comparison of the UV traces for samples with different concentrations indicated more concentrated samples to elute earlier, suggestive of self-association (Figure 4D). Furthermore, the molar masses determined by MALS indicated two populations of UBQLN1 eluting within a single UV peak, with the earliest eluting part of the peak displaying a relatively flat mass profile at the expected 8.93 kDa monomeric mass and the later eluting component of the peak exhibiting curvature and elevated mass (Figure 4D). The curvature feature mimics the complex of S100B with p53 (293–393, L344P)[45] and was attributed to dynamic exchange between the free and bound states. In the case of UBQLN1 (514–589, F547Y), we expect the curvature to be caused by dynamic exchange between monomeric and self-associated states.

We hypothesized that the UBAA portion of UBQLN1 might cluster with the hydrophobic side of its amphipathic helix occluded from the aqueous solvent. We used AlphaFold2-Multimer[46] to generate model structures of UBQLN1 (514–589) oligomers at various stoichiometries. These structures all predict UBAA to form a helical bundle with the UBA protruding outward (Figure 4E).

To evaluate further the possibility of dynamic exchange between oligomerization states in UBAA and the effect of the AZUL domain on such exchange, we acquired CPMG R_2 relaxation dispersion data at 850 and 600 MHz on ^{2}H-^{15}N-UBQLN1 (514–589, F547Y) with and without AZUL present (Figure S4A–B). As expected, field-dependent effects were observed, with greater R_{ex} (chemical exchange contribution to the apparent R_2) at the higher field. The helical region of UBAA was found to undergo exchange in the absence of the AZUL at 850 MHz (Figure S4A) and this exchange also occurred with AZUL present (Figure S4B). Therefore, the UBAA undergoes intrinsic chemical exchange that is independent of the AZUL interaction.

To better compare the effects with and without AZUL, we plotted the 850 MHz R_{ex} data from both samples side-by-side for each residue to find similarity between the two samples in the UBAA region, and AZUL-dependent effects in the UBA region (Figure 4F). Increased R_{ex} was observed for UBA residues when AZUL was present (Figure S4), particularly G558 and A578 (Figure 4F). These data indicate AZUL-dependent exchange in UBA, suggesting this as the site of interaction, and intrinsic chemical exchange in UBAA, supportive of its dynamic self-association.

E6AP AZUL interacts with UBQLN UBA

We next sought to test directly which part of UBQLN1/2 interacts with E6AP AZUL. We titrated unlabeled E6AP AZUL into ~0.1 mM ^{15}N-labeled UBQLN1 (514–586) and recorded 2D ^{15}N-dispersed HSQC spectra. UBQLN1 (514–586) lacks amino acids with absorbance at 280 nm and we therefore estimated the protein concentration by 1D NMR spectra and Coomassie staining. We observed signal shifting in the ^{1}H, ^{15}N-HSQC spectrum of ^{15}N-labeled UBQLN1 (514–586) upon addition of E6AP AZUL (Figure 5A), consistent with binding and quantified these effects for each backbone amide nitrogen and hydrogen signal in UBQLN1 (514–586). The values were plotted across the UBQLN1 sequence to identify amino acids that were significantly affected by AZUL binding (Figure 5B). We found the affected residues to map to three main areas: UBA α3, the linker between the UBA helices α1 and α2, and a residue cluster in UBAA (H527-G535) (Figure 5B). This information is mapped onto a model monomeric structure of UBQLN1 in Fig 5C.

To directly test the importance of UBA for UBQLN interaction with AZUL, we used the UBQLN2 condensate assay from Fig 2E–F. Initially, we wanted to remove UBA from UBQLN2 and test whether AZUL still associates with UBQLN2 condensates in its absence. However, based on previous reports, we expected UBA removal to negatively impact the ability of UBQLN2 to form condensates[32]. It was also reported, however, that removal of UBL in addition to UBA (i.e., ΔUBLΔUBA) increases UBQLN2 condensate formation ability[32]. Therefore, we purified UBQLN2 ΔUBLΔUBA (109–576) to assess the contribution of the UBQLN2 termini in the recruitment of E6AP AZUL to UBQLN2 condensates. When AZUL-mEGFP was mixed with UBQLN2 ΔUBLΔUBA, we found the AZUL-mEGFP to be excluded from the condensates (Figure 5D), suggesting that UBA (and/or UBL) is contributing to the recruitment of AZUL-mEGFP to UBQLN2 condensates.

We noted that the UBQLN1 UBA residues that shift upon AZUL addition were similar to those identified in UBQLN2 as interacting with UBL[32]. Based on these similar binding surfaces, we hypothesized that E6AP AZUL might compete with UBQLN UBL for binding to its UBA. To test this model, we purified ^{15}N-UBQLN2 UBL and titrated in unlabeled E6AP AZUL, UBQLN1 (514–589, F547Y), or the two binding partners together. Addition of E6AP AZUL did not cause spectral changes to UBQLN2 UBL, indicating that the AZUL does not interact with UBL (Figure 5E). Of note, a previous report suggested that E6AP and UBQLNs might be able to interact through the UBQLN1/2 UBL[47]; this result suggests that the binding observed in the previous report is not mediated through AZUL. By contrast, UBQLN1 (514–589, F547Y) induced spectral shifting of ^{15}N-UBQLN2 UBL signals, indicating binding. Addition of E6AP AZUL to the ^{15}N-UBQLN2 UBL:UBQLN1 (514–589, F547Y) mixture, however, caused back-shifting of myriad UBQLN2 signals (Figure 5E), suggesting E6AP AZUL competes for the UBL binding site of the UBA domain, albeit with weaker affinity.

A previous report found the affinity of the UBQLN2 UBL:UBA interaction to be ~200 μM[32], and sequence conservation between the UBQLN1 and UBQLN2 UBA regions (Figures 1A and S1B) suggests a similar affinity for the UBQLN2 UBL:UBQLN1 UBA interaction. Since AZUL was only partially able to compete away UBA from UBL, we anticipated that the dissociation constant (K_d) of the UBQLN1:AZUL interaction is higher than 200 μM. We used the shifting of proton amide signals ($\Delta\delta_H$) by titration of unlabeled AZUL into 50 μM ^{15}N-UBQLN1 (514–589, F547Y) to estimate the K_d value for this interaction[48]. This analysis revealed distinct values for UBA and UBAA residues; for UBA, we found the K_d to be ~460 μM (Figure S5A), consistent with the competition experiment data of Figure 5E. A weaker K_d value of ~1 mM was measured for the UBAA domain (Figure S5A).

As a further test that the UBA is in fact the region interacting with E6AP AZUL, we purified UBQLN1 UBA (541–589) and added it to ^{15}N-AZUL. We observed chemical shift perturbations in ^{15}N-AZUL upon UBQLN1 UBA addition (Figure 5F and Fig S5B) similar to those observed upon addition of UBQLN1 (514–589, F547Y) (Figures S2A and 2A). Together, these data indicate that UBA interacts directly with AZUL. Figure S5C illustrates how E6AP interaction with the UBQLN UBA may occur, given our finding that the AZUL is recruited to UBQLN2 condensates (Figure 2G), and taking into account our findings that UBAA undergoes dynamic self-association.

NOE interactions confirm direct binding of AZUL to UBQLN1 UBA

To unambiguously determine the AZUL:UBQLN1 binding interface, we performed a ^{15}N-edited NOESY experiment on uniformly labeled ^{2}H-^{15}N-UBQLN1 (514–589, F547Y) mixed with 2-fold molar excess unlabeled AZUL (as used in Figures 3C, 4B, and 4F). This experimental set-up detects intermolecular interactions between AZUL aliphatic and UBQLN1 amide protons (Figure S6A), as well as intramolecular interactions in UBQLN1 that involve exchangeable protons[49]. Interactions between the UBQLN1 amide protons were readily detected as expected (data not shown), as well as those involving UBQLN1 T572 Hγ1 (Figure S6B), which likely forms a hydrogen bond to a nearby backbone carbonyl from A568, L569, or D575 (Figure S6C). Additional NOEs were detected to the backbone amides of UBQLN1 F559 and E581, as well as to the UBQLN1 sidechain amide of N577 (Figure 6A), which localize to the third helix and loop between helices 1 and 2 of UBQLN1 UBA. These regions were also implicated in AZUL binding by the titration experiments and exchange analyses (Figure 5A–C). We were unable to detect any NOEs to the UBAA region.

The weakness and paucity of intermolecular NOEs is consistent with the measured weak binding affinity (Figure S5A). To further assess binding in a manner more suited for weak interactions, we performed saturation transfer experiments with the same sample. We chose saturation values based on the observed NOEs from Figure 6A (0.915 and 1.439 p.p.m.) and measured peak intensity for each UBQLN1 backbone and sidechain amide with and without the saturation. Plotting the intensity reduction ratio ($1- I_{sat}/I_{ref}$) from this analysis revealed the regions around F559 and E581 to show the greatest effect from the saturation transfer (Figure 6B), consistent with the detected steady state NOEs (Figure 6A). Most of the sidechain amides were overlapped, prohibiting their analyses; however, N577 and a few other sidechains were not overlapped. We were similarly able to observe the N577 sidechain undergoing large intensity reduction indicating interaction with AZUL (Figure 6B). Altogether, our data indicate that UBQLN1 F559, N577, and E581 are at the AZUL binding interface.

An AlphaFold-NMR integrated structure elucidates AZUL:UBQLN1 binding mechanism

We next sought to assign the intermolecular NOEs (Figure 6A) to AZUL atoms by using the deposited chemical shift assignments of apo AZUL[12] and of RAZUL-bound AZUL[13]. We were able to identify candidate AZUL atoms for the observed NOEs, however we were concerned by the likelihood that the AZUL signals might have shifted upon binding to UBQLN1. To bolster confidence in AZUL assignments, we used AlphaFold2-Multimer to predict structures of the UBQLN1:AZUL complex. Consistent with our experimental data, AlphaFold predicted binding between the AZUL and UBQLN1 UBA domain. The top scoring structures converged to a model in which the N-terminus of helix 1 in AZUL is close to N577 of UBQLN1, and helix 2 of AZUL is proximal to F559 and E581 (Figure S7A). This prediction fit our NMR data well (Figure 2A–C, S2A, 4F, 5A–C, and 6A–B), with NOEs shared by UBQLN1 F559 and E581 fitting to the chemical shift values of methyl groups from AZUL L73, which is positioned between these two residues in the predicted structures (Figure S7A). In addition, the NOEs detected to the sidechain amide of UBQLN1 N577 fit to the chemical shift values of the beta and delta hydrogens of AZUL R26, which is nearby in the predicted structures. We next used these intermolecular NOE assignments (as labeled in Fig 6A) to generate distance constraints that were used in the program Xplor-NIH[50] to calculate structures for the AZUL:UBQLN1 complex. The structure that best matched the experimental data was similar to that predicted by AlphaFold2-Multimer, but with AZUL rotated slightly. This rotation places AZUL L73 between F559 and E581, and positions AZUL K77 closer to E581 (Figure 6C and Fig S7B).

Interestingly, in the AlphaFold-predicted UBQLN1 oligomer structures (Figure 4E), all models place UBA and the E6AP-binding site in an outward-directed orientation, with the AZUL-binding surface exposed. We modeled AZUL onto the UBQLN1 AlphaFold-predicted tetramer (Figure 7A) to find that adjacent AZUL molecules experience steric clashes. We therefore inputted four UBQLN1 and AZUL molecules into AF2-Multimer to examine whether the predicted UBQLN1 conformation is altered by the presence of AZUL. The AlphaFold-predicted structures with AZUL were less convergent than the ones with UBQLN1 alone, but each was shifted in the UBAA packing to accommodate the binding of AZUL (compare Fig 7B to 7A). Based on this modeling, we expect that the observed chemical exchange in UBAA caused by AZUL addition may be driven by steric restrictions involving AZUL binding that alter the UBAA mode of self-association.

Discussion

In this study, we discover that E6AP interacts with UBQLN1 and UBQLN2 *in vitro* and *in cellulo* and establish a structural model of their interaction by using AlphaFold2-Multimer in combination with intermolecular NOESY data. While we do not have any data investigating whether the E6AP AZUL also interacts with other UBQLNs, we expect the AZUL may also interact with UBQLN3 and UBQLN4 based on high sequence similarity in the region of interaction. We find that although UBQLN interaction with AZUL is weak, UBQLN2 recruits AZUL to its condensates. Characterizing weak protein-protein interactions structurally is challenged by their dissociation while under study; weak interactions cannot be captured by crystallization and have yet to be trapped for study by cryo-electron microscopy approaches. In contrast, NMR is performed in solution and sensitive to changes in chemical environment, including those induced by weak interactions, allowing the study of highly dynamic and transient protein-protein binding events.

We previously found that AlphaFold2 is unable to predict structural defects caused by missense mutations[51]; however, this study shows benefits of using AlphaFold to accelerate and complement NMR data acquired on protein complexes and this application of AlphaFold may be particularly important for weakly interacting systems. We establish an NMR-AlphaFold pipeline that can be applied to other systems to accelerate NMR data analyses and overcome barriers of using NMR for structure calculations by implementing AlphaFold2-Multimer modeling as an independent tool to aid intermolecular NOE assignments, akin to previous efforts in which AlphaFold models were used to aid the solution of crystal structures[52–56]. We outline the workflow taken to achieve our final structural model in Fig 7C.

The prospect of E6AP interacting with UBQLN2-containing condensates within cells as suggested by our *in vitro* data is an intriguing one, considering that condensates have the ability to increase local concentrations (allowing weaker affinity interactions) and enzymatic rates[57]. In this model, it is possible that E6AP interacts with UBQLN proteins at known cellular condensates/membraneless organelles, such as stress granules. Considering that UBQLN2 is enriched in brain and both UBQLN2 and E6AP are implicated in neurological disorders/diseases, another possibility is that they interact predominantly in brain-specific condensates, such as those observed at nerve-terminals[58,59].

UBQLN1 binds to its substrates through a region in the middle of the protein sequence[26] and we propose that E6AP AZUL binding to UBQLN UBA co-localizes this E3 for ubiquitination of UBQLN cargo (Figure 7D). E6AP catalyzes the formation of K48-linked ubiquitin chains and our data suggest that the weaker interaction of UBQLN UBA with E6AP AZUL would be replaced by UBQLN UBA:ubiquitin interactions (Figure 7D). UBQLN-bound ubiquitinated substrates could either bind to substrate receptors in the proteasome through ubiquitin interactions[60] or through the UBQLN UBL domain[34,35,61]. At the proteasome, further ubiquitination could occur by RAZUL-associated E6AP[13], remodelling ubiquitin chains on substrates for more efficient degradation.

Our data also suggest that AZUL binding to UBQLN1 UBA leads to rearrangement of UBAA self-association/oligomerization. Consistent with these findings, a recent publication found ubiquitin chain binding to the UBQLN2 UBA induces small shifts in the NMR signals of amino acids in the region of UBQLN2 homologous to UBAA, with the magnitude of shifting dependent on chain linkage type (i.e. M1, K11, K48, K63)[33]; this finding suggests chain type-dependent UBAA reorganization. Thus, either ubiquitin or E6AP AZUL binding to UBQLN UBA appears to be sensed at the UBQLN UBAA domain.

Our studies reported here provide clarity to previous findings and expand upon others to develop our understanding of the role of shuttle factors and E6AP in proteasome biology. In particular, association of an E3 ligase with the UBQLN UBA region has been previously proposed based on UBQLN1 UBA-dependent ubiquitination of a substrate in

HEK cytosol and in a reconstructed setting with UBQLN1-bound substrate purified from rabbit reticulocyte lysate[26]. Our findings reported here suggest that this E3 ligase is likely to be E6AP. In addition, there is growing appreciation for the role of shuttle factors in condensate formation, and E6AP has also been shown regulate the number of nuclear condensates formed in response to hyperosmotic stress[20]. While the role of condensates for proteasome function is still debated, our findings connecting E6AP with UBQLN1/2 provide evidence for tight integration of E3 ligase activity with proteasome shuttle factors and a possible regulatory role for regions that drive dynamic oligomerization.

STAR Methods

RESOURCE AVAILABILITY

Lead contact—Further information and requests for resources and reagents should be directed to and will be fulfilled by the lead contact, Kylie J. Walters (kylie.walters@nih.gov).

Materials availability—Plasmids generated by this study are available upon request.

Data and code availability—NMR chemical shift assignments have been deposited at the Biological Magnetic Resonance Data Bank (BMRB) and are available as of the date of publication. Accession numbers are listed in the key resources table.

This paper does not report original code.

Any additional information required to reanalyze the data reported in this paper is available from the lead contact upon request.

EXPERIMENTAL MODEL AND SUBJECT DETAILS

Bacterial cell cultures—The strains of *Escherichia coli* used for DNA propagation and protein expression are indicated in the key resources table. For DNA propagation and expression of unlabeled proteins, cells were grown in Luria-Bertani Broth (LB; 10 g/L Tryptone; 5 g/L Yeast Extract; 10 g/L NaCl) supplemented with appropriate antibiotics. For DNA propagation, cells were grown at 37 °C with shaking. For protein expression, cells were grown at 37 °C with shaking until they reached OD_{600} 0.5–0.6, at which point they were induced with 0.4 mM IPTG and maintained at 17 °C overnight. For isotopically labeled proteins, cells were grown in M9 minimal media with ^{15}N NH_4Cl as the only nitrogen source and/or ^{13}C glucose as the only carbon source. For uniform deuteration, cells were transitioned from LB to M9 media containing 70% D_2O, and then 100% D_2O M9 media containing D7-labeled glucose as the only carbon source and ^{15}N NH_4Cl as the only nitrogen source with 10 mL of BioExpress cell growth media (U-D, 98%; U-^{15}N, 98%, 10x concentrate) spiked in per liter of culture.

Mammalian cell cultures—The mammalian cell lines used in this study are all male (see key resources table). HCT116 cells (human colorectal carcinoma cells derived from an adult male) and ΔRAZUL (clone 13) cells (generated from HCT116 cells as described previously[13]) were maintained at 37 °C and 5% CO_2 in McCoy's 5A medium supplemented with 10% FBS. Cells were grown and maintained in standard tissue culture plates.

METHOD DETAILS

Cell culture, crosslinking, and immunoprecipitations—All mammalian cell lines were grown in McCoy's 5A modified medium (Thermo Fisher Scientific 16600082), containing 10% fetal bovine serum (Atlanta Biologicals S12450), and maintained at 37 °C and 5% CO_2. The HCT116 cell line was purchased from the ATCC (CCL-247) and ΔRAZUL (clone 13) was described previously[13]. For crosslinking, cells were washed 2× at room temperature (RT) with PBS containing calcium and magnesium pH 7.2 (PBS/Ca/Mg) (either made by hand or Sigma D1283 diluted to 1× and pH'd to 7.2) and incubated with 2 mM DSP (ChemScene CS-0068460, first resuspended in DMSO to 25 mM, then diluted to 2 mM in PBS/Ca/Mg) for 30 min at RT. DSP was aspirated off and residual DSP was quenched through addition of 20 mM Tris (diluted from a 1 M stock) in PBS/Ca/Mg for 15 min at RT. Tris/PBS/Ca/Mg was aspirated off and cells were harvested in Nonidet P-40 lysis buffer (0.5% Nonidet P-40, 50 mM Tris pH 7.5, 150 mM NaCl, 1 mM PMSF, 5 μg/mL Pepstatin A, 10 mM Sodium Pyrophosphate, 10 mM NaF, 1 mM Sodium Vanadate, and Roche EDTA-free protease inhibitor tablet). Following 20,000 g centrifugation at 4 °C, lysate supernatants were quantitated with Pierce 660 nm protein assay reagent (Thermo Scientific 22660). For IP, 2 mg of protein was combined with 15 μL anti-UBQLN1 (Cell Signaling Technology 14526, RRID:AB_2798502) or anti-UBQLN2 (Cell Signaling Technology 85509, RRID:AB_2800056) antibodies, or 6 μL anti-E6AP (ProteinTech 10344–1-AP, RRID:AB_2211801) antibody, or equivalent μg of control rabbit IgG (2 μg for E6AP IP or 1.815 μg for UBQLN1/2 IPs). Antibody-lysate complexes were allowed to incubate overnight at 4°C with end-over-end tumbling. 50 μL of Protein A Dynabeads (10002D) were added to the antibody-lysate mixtures and allowed to incubate for another 3 hours at 4°C with end-over-end tumbling. Bead-antibody complexes were washed 5× in Nonidet P-40 lysis buffer and eluted at 95 °C in 2x sample buffer (100 mM Tris pH 6.8, 4% SDS, 200 mM DTT, 20 % glycerol, 4 M urea, 0.0125% bromophenol blue).

SDS-PAGE, antibodies, and immunoblots—Protein lysates and immunoprecipitates were subjected to SDS-PAGE on 4–12% NuPAGE Bis-Tris gels (Thermo Fisher Scientific NP0322) using MOPS SDS running buffer (Thermo Fisher Scientific NP0001). Proteins were transferred to 0.45 μm nitrocellulose membranes (GE/Cytiva Amersham 10600003) using NuPAGE transfer buffer (Thermo Fisher Scientific NP00061) containing 10% methanol. Membranes following transfer were blocked with 7% milk in tris buffered saline with 1% tween 20 (TBS-T). Blocked membranes were incubated overnight at 4 °C with primary antibodies diluted 1:1,000 in 7% milk in TBS-T. Membranes were washed five times in TBS-T and incubated with HRP-conjugated secondary antibodies diluted in 7% milk in TBS-T for 2 h. Following another five washes, blots were developed using WesternBright ECL-spray (Advansta K-12049-D50) and labForce HyBlot CL Autoradiography Film (Thomas Scientific 1141J52). Primary antibodies used were: E6AP (Sigma E8655), UBQLN2 (Novus Biologicals NBP2–25164), UBQLN1 (Cell Signaling Technology 14526), and hRpn10 (Cell Signaling Technology 3336). Secondary antibodies used were Sigma A9917 (anti-mouse, 1:5,000) and Sigma R3155–200UL (native rabbit secondary, 1:1,000).

Protein expression and purification—The following constructs were purchased through GenScript with codon optimization for expression in *E. coli*: UBQLN1, UBQLN1 (514–586), UBQLN1 (514–589, F547Y), UBQLN1 UBA (541–589), UBQLN2, UBQLN2 ΔUBLΔUBA (109–576), and AZUL-mEGFP (E6AP isoform II 24–87 with a C-terminal mEGFP). All constructs except for UBQLN1 (514–586) and UBQLN1 (514–589, F547Y) were inserted into the pGEX-6P-1 vector between the PasI and XhoI sites, in frame with an N-terminal glutathione S-transferase (GST) and a PreScission protease cleavage site. The UBQLN1 UBA construct contains a tyrosine residue in the tag to enable quantitation at A_{280}. UBQLN1 (514–586) and UBQLN1 (514–589, F547Y) were inserted into the pGEX-6P-3 vector between the EcoRI and XhoI sites. The UBQLN2 ΔUBLΔUBA (109–576) construct contains an N-terminal mCherry separated from the UBQLN2 sequence by a thrombin protease cut site; however, the mCherry was found to inhibit condensate formation of the attached UBQLN2 ΔUBLΔUBA and was therefore removed via thrombin digestion after purification described below, followed by an additional run over a Superdex75 on an FPLC system to remove the mCherry. The mEGFP in frame with AZUL in the AZUL-mEGFP (separated by a TEV protease cut site) plasmid is based on the EGFP sequence, but additionally contains the A206K mutation (numbered relative to avGFP, A207K relative to EGFP). Plasmids were transformed into *E. coli* strain BL21 (DE3) (Thermo Fisher Scientific C600003) with ampicillin selection. Transformed cells were grown at 37 °C to OD_{600} of 0.5–0.6 and induced with 0.4 mM IPTG at 17 °C overnight. For AZUL-mEGFP, zinc sulfate was added at the time of induction to a final concentration of 20 μM. Bacteria were pelleted via centrifugation at 4,000 rpm at 4 °C for 40 minutes, using a Beckman Coulter J6-M1 centrifuge with a JS-4.2 rotor, and stored at −80 °C until purification. Frozen bacteria containing full-length or ΔUBLΔUBA UBQLN constructs were resuspended in Buffer A (50 mM Tris pH 8, 1 mM $MgCl_2$, 1 mM PMSF, and 0.2 mg/mL DNase I and Roche Complete Mini protease inhibitor cocktail), which intentionally contains no NaCl to avoid condensate formation during purification. In the case of UBQLN2 full-length protein, 0.5 mM EDTA was included in all purification buffers, but was removed by desalting with a Zeba desalting column (Thermo Scientific 89890). AZUL-mEGFP was resuspended in Buffer B (10 mM MOPS at pH 7.2, 300 mM NaCl, 5 mM 2-mercaptoethanol, 10 μM zinc sulfate, and EDTA-free protease inhibitor cocktail (Roche Diagnostics 11836170001)). UBQLN1 (514–586), UBQLN1 (514–589, F547Y) and UBQLN1 UBA (541–589) constructs were resuspended in Buffer C (20 mM at Tris pH 7.6, 300 mM NaCl, 5 mM DTT, and Roche Complete Mini protease inhibitor cocktail (Roche Diagnostics 11836153001)). Resuspended bacteria were lysed via sonication and centrifuged at 15,000 rpm (~27,216g) for 30 min at 4 °C. Supernatants were incubated with pre-washed glutathione sepharose beads (Cytiva 17-0756-05) for 3 hours at 4 °C with a fresh protease inhibitor cocktail tablet added. Beads were washed 4–5 times in Buffer A (or B, for AZUL-mEGFP; or C, for UBQLN1 (514–586), UBQLN1 (514–589, F547Y), and UBQLN1 UBA (541–589)) and incubated overnight with PreScission protease to separate proteins from the GST tag. The on-bead PreScission protease digestion was inefficient for AZUL-mEGFP, so in this case, GST-AZULmEGFP was eluted with 20 mM Glutathione in Buffer D (20 mM $NaPO_4$ at pH 6.8, 50 mM NaCl, 5 mM 2-mercaptoethanol, 10 μM zinc sulfate), and incubated overnight again with PreScission protease. Proteins released from GST were purified further through size exclusion chromatography on an ÄKTA pure FPLC system (Cytiva) using a HiLoad 16/600 Superdex200 or Superdex75 prep grade column in 20 mM $NaPO_4$, pH 6.8 (UBQLN1, UBQLN2 and UBQLN2 ΔUBLΔUBA) or Buffer D (AZUL-mEGFP) or Buffer E (10 mM MOPS at pH 6.5, 50 mM NaCl, 5 mM DTT, and 10 μM zinc sulfate) (UBQLN1 (514–586), UBQLN1 (514–589, F547Y), and UBQLN1 UBA (541–589)). The AZUL-mEGFP required one additional incubation with glutathione beads to remove free GST.

The plasmid encoding E6AP AZUL (E6AP isoform II 24–87) was generated previously[13]. E6AP AZUL was transformed into *E. coli* strain BL21(DE3) under kanamycin selection and grown at 37 °C until OD_{600} of 0.5–0.6 at which point zinc sulfate was added to a concentration of 20 μM and expression induced through addition of IPTG to 0.4 mM. Following induction, the cells were incubated with shaking overnight at 17 °C. Cells were pelleted as above and resuspended in Buffer F (10 mM MOPS pH 6.5, 450 mM NaCl, 10 μM zinc sulfate, and 5 mM β-mercaptoethanol). Resuspended cells were sonicated and centrifuged as above, and supernatant incubated with Ni-NTA beads (Qiagen) for 1 hour at 4 °C. Ni-NTA beads were washed 3 times with Buffer F and 2 times in Buffer G (10 mM MOPS pH 6.5, 450 mM NaCl, 10 μM zinc sulfate, 20 mM Imidazole, and 5 mM β-mercaptoethanol). Ni-NTA beads were incubated with 150 μL of 1 Unit/μL thrombin protease (EMD MILLIPORE catalog #605195–1000U) in Buffer F overnight at 4 °C with agitation. E6AP AZUL was eluted from the Ni-NTA beads 6 times with Buffer E, the eluant combined, concentrated to <2mL, and separated on an FPLC system with a Superdex 75 column in Buffer E.

UBQLN2 UBL (UBQLN2 26–103) was sub-cloned into the pGEX-2T vector between the BamHI and EcoRI sites and expressed in *Escherichia coli* strain BL21 (DE3) as fusion proteins with GST and a thrombin protease cleavage site, as was done previously[35,62]. Cells were grown at 37°C to OD_{600} of 0.5 – 0.6 and protein expression induced overnight at 17°C by addition of 0.4 mM IPTG. The cells were frozen in liquid nitrogen and stored at −80°C for ~4 hrs, followed by resuspension in Buffer H (20 mM Tris at pH 7.5, 300 mM NaCl, 2 mM DTT) supplemented with Roche Complete protease inhibitor cocktail tablets. Resuspended bacteria were lysed via sonication and centrifuged at 15,000 rpm (~27,216g) for 30 min at 4 °C. Supernatants were incubated with pre-washed glutathione sepharose beads (Cytiva 17-0756-05) for 3 hours at 4 °C with a fresh protease inhibitor cocktail tablet added. Beads were washed 4–5 times in Buffer H and incubated overnight with 150 μL of 1 Unit/μL thrombin protease (EMD MILLIPORE catalog #605195–1000U) to separate proteins from the GST tag. UBQLN2 UBL was eluted from the glutathione sepharose beads 6 times with Buffer H, the eluant combined, concentrated to <2mL, and separated on an FPLC system with a Superdex 75 column in Buffer I (20 mM $NaPO_4$ at pH 6.5, 50 mM NaCl, 2 mM DTT). The sample was then dialyzed 3 times against 1 L of Buffer E at 4 °C.

^{15}N ammonium chloride, ^{13}C glucose, D-glucose-1,2,3,4,5,6,6-d_7 (97–98%), and $^{2}H_2O$ (Cambridge Isotope Laboratories) were used for isotope labeling. ^{2}H,^{15}N-UBQLN1 (514–589, F547Y) was expressed similar to as was done previously for PUT3[49], with cultures being equilibrated to 70% D_2O for 24 hours, 100% D_2O for 24 hours, and then 100%

D_2O with ^{15}N ammonium chloride, D7 glucose and 20 mL BioExpress cell growth media (Cambridge Isotope Laboratories CGM-1000-DN) per liter added. Based on the mass from LC-MS, deuterium labeling of UBQLN1 (514–589, F547Y) was estimated to be >95%.

NMR samples and experiments—NMR samples were prepared, namely 1) 0.35 mM ^{15}N, ^{13}C, 80% ^{2}H-labeled UBQLN1 (514–586); 2) 0.05 mM ^{15}N-labeled E6AP AZUL; 3) 0.05 mM ^{15}N-labeled UBQLN1 (514–589, F547Y); 4) 0.6 mM ^{15}N-labeled UBQLN1 (514–589, F547Y); 5) 0.05 mM ^{15}N-labeled UBQLN2 UBL; 6) 0.1 mM ^{15}N-labeled UBQLN1 (514–586); 7) 0.6 mM ^{2}H-^{15}N-UBQLN1 (514–589, F547Y) with 1.2 mM unlabeled AZUL.

2D ^{1}H-^{15}N HSQC and ^{1}H-^{13}C HSQC spectra and 3D HNCACB/CBCA(CO)NH, HNCO/HN(CA)CO, ^{15}N-edited NOESY-HSQC (200 ms mixing time), and ^{13}C edited NOESY-HSQC spectra (150 ms mixing time) were recorded on sample 1. ^{15}N-edited NOESY-HSQC (120 ms mixing time) was recorded on sample 4. Samples 2, 3, 5, and 6 were used in 2D ^{1}H-^{15}N HSQC titrations. Sample 7 was used for ^{15}N-edited NOESY-HSQC (1.8 s recycle delay and 200 ms mixing time) and saturation transfer experiments. Selective saturation of AZUL aliphatic protons in the saturation transfer experiments was performed with a 15-ms IBURP2 pulse centered at 0.915 or 1.439 ppm (2.5 s saturation duration and 3.5 s recycle delay). I_{ref} measurements were taken from a spectrum in which the 2.5 s irradiation was focused at −10 ppm. All NMR experiments were conducted in Buffer E (10 mM MOPS at pH 6.5, 50 mM NaCl, 5 mM DTT, 10 μM zinc sulfate, 1 mM pefabloc, 0.1% NaN_3, and 5% $^{2}H_2O$/95% $^{1}H_2O$), except for 2D ^{1}H-^{13}C HSQC and ^{13}C-edited NOESY-HSQC experiments, which were acquired on samples dissolved in $^{2}H_2O$. All NMR experiments were conducted at 25°C. Spectra were recorded on Bruker AvanceIII 600, 700, 800, 850, or 900 MHz spectrometers equipped with cryogenically cooled probes.

All NMR data processing was performed using NMRpipe[63] and spectra were visualized and analyzed with XEASY[64]. Secondary structure was assessed by the TALOS+ program[44].

NMR titration experiments—^{1}H, ^{15}N HSQC experiments were recorded on samples 2, 3, 5 and 6 (^{15}N-labeled E6AP AZUL, UBQLN1 (514–589, F547Y), UBQLN2 UBL, and UBQLN1 (514–586)) with increasing molar ratio of unlabeled ligand (UBQLN1 (514–586), UBQLN1 (514–589, F547Y) or E6AP AZUL), as indicated. The amide nitrogen and hydrogen chemical shift perturbations (CSP) were mapped for each amino acid either with hydrogen and nitrogen values recorded separately, or according to Equation 1.

$$CSP = \sqrt{0.2\Delta\delta_N^2 + \Delta\delta_H^2} \tag{1}$$

$\Delta\delta_H$, change in amide proton value (in parts per million); $\Delta\delta_N$, change in amide nitrogen value (in parts per million).

NMR relaxation experiments—Rates for ^{15}N longitudinal R_1 and transverse R_2 relaxation and magnitudes of the hetNOE were recorded on 0.05 mM and 0.6 mM ^{15}N-labeled UBQLN1 (514–589, F547Y) and 0.6 mM ^{2}H-^{15}N-UBQLN1 (514–589, F547Y) with 1.2 mM unlabeled AZUL at 25°C and 700 MHz with a cryogenically cooled probe. R_1 and R_2 were derived by fitting data acquired with different relaxation delays (10, 20, 40, 50, 60, 80, 110, 160, 240, 320, 400, 600, 800, 1000, and 1200 ms for longitudinal relaxation; 10, 20, 30, 50, 70, 90, 110, 130, and 150 ms for transverse relaxation) to a single-exponential decay function, and error values were determined by repeating one data point. Relaxation rates were fitted by using NMRFAM-Sparky[65]. Two spectra were recorded for steady-state NOE intensities, one with 4s of proton saturation to achieve the steady-state intensity and the other as a control spectrum with no saturation to obtain the Zeeman intensity. The control spectrum was repeated to determine error values. hetNOE were then calculated from the ratio described in Equation 2, as described in[66].

$$\text{hetNOE} = \left(\frac{\gamma_{\mathrm{H}}}{\gamma_{\mathrm{N}}}\right)\left[\frac{R_N\left(H_Z^N \leftrightarrow N_Z\right)}{R_N\left(N_Z\right)}\right] \tag{2}$$

Constant Time CPMG R_2 Relaxation Dispersion experiments were performed on 0.6 mM ^{15}N-labeled UBQLN1 (514–589, F547Y) and 0.6 mM ^{2}H-^{15}N-UBQLN1 (514–589, F547Y) with 1.2 mM unlabeled AZUL at 25°C on 600 MHz and 850 MHz NMR spectrometers using the Bruker pulse sequence hsqcrexetf3gpsi3d with the total relaxation delay $Tcp = 40$ ms. Spectra were recorded with CPMG effective fields, v_{CPMG}, of 25, 50, 75, 100, 150, 200, 250, 300, 400, 500, 600, 700, 800, 900, 1000, 1100, 1200, 1300, and 1400 Hz. Spectra were processed using NMRPipe and peak intensities were measured from the sum of a 3 × 3 grid centered on the peak center. Effective R_2 rates $\left(R_2^{eff}\right)$ at each v_{CPMG} were determined using the relation $R_2^{eff}(\upsilon_{CPMG}) = \frac{1}{Tcp}\ln\left(\frac{I(\upsilon_{CPMG})}{I_0}\right)$.[67] where $I(v_{CPMG})$ is the peak intensity after the Tcp relaxation period at a particular v_{CPMG} and I_0 is the peak intensity without a Tcp relaxation period. R_2 relaxation dispersion profiles were fit to the Carver-Richards equation[68–70] using the fmin function from the SciPy 1.7.1 package in Python 3.9. Errors in the exchange parameters were determined by using the Monte-Carlo method with a minimum of 2% R_2^{eff} error and 100 synthetic data sets.

To select only the residues from the Carver-Richards fitting that show significant chemical exchange as well as fit to a two-site model, an F-test analysis was used as previously described[71]. In brief, the R_2 relaxation dispersion data were fit to both the Carver-Richards equation and a model that neglects exchange (optimizes for R_2^0 From the selected residues, the chemical shift at 600MHz and 850MHz only) and the F statistic was calculated for each residue. Residues were selected as undergoing chemical exchange if: 1) the F-test showed significant improvement (p < 1%) of the Carver-Richards equation over the equation that neglects exchange and 2) the $R_2^{eff}(\upsilon_{CPMG} = 25\text{Hz}) - R_2^{eff}(\upsilon_{CPMG} = 1400\text{Hz}) > 3s^{-1}$. From the selected residues, the chemical shift difference between exchanging sites, Δω, was extracted and compared to chemical shift perturbation results derived from titration experiments.

***In vitro* biomolecular condensate assays—**UBQLN2 constructs and AZUL-mEGFP or EGFP were mixed at the indicated concentrations and 50 μL of the mixture was added to an Ibidi μ-Slide (Cat.No. 81506 or 81507, incubated with 3% BSA for 15 min and washed 3× with water) and imaged at 37°C on a Zeiss LSM710 Laser scanning confocal microscope with a 63× oil, 1.4 NA, 0.19 mm objective. Images were processed using Fiji[72]. EGFP for control experiment shown in Fig 6B was purchased from Chromotek (EGFP-250) and run through a Zeba desalting column (Thermo Scientific 89890) to exchange into 20 mM $NaPO_4$ pH 6.8, 200 mM NaCl.

Circular dichroism—Far-UV range CD spectra (260–190 nm) of 10 μM UBQLN1 (514–589, F547Y), 10 μM AZUL, and 10 μM UBQLN1 (514–589, F547Y) mixed with AZUL at a 1:1 ratio were recorded on a Jasco J-1500 CD spectrometer using a quartz cuvette with 1.0 mm path length and temperature controlled at 25 ± 0.1°C. Buffer J (10 mM MOPS at pH 6.5, 10 mM NaCl, 0.5 mM DTT, 10 μM zinc sulfate) was used as a control. All spectra were collected continuously at a scan speed of 20 nm/min and averaged over accumulation of three spectra. The buffer spectrum was subtracted from the protein spectra during data analyses. Secondary structure analysis was conducted with the program CONTIN[73,74] by the DichroWeb server[75] using reference dataset SP175t (190–240 nm)[76].

SEC-MALS—SEC-MALS data were collected by an Ultimate 3000 HPLC (Thermo Scientific) in-line with an Ultimate 3000 UV detector (Thermo Scientific), miniDawn MALS detector, and Optilab refractive index detector (Wyatt Technology). The data were collected following in-line fractionation with a WTC-010S5 (7.8 × 300 mm) 100 Å pore size SEC analytical column (Wyatt Technology), pre-equilibrated in Buffer E (10 mM MOPS at pH 6.5, 50 mM NaCl, 5 mM DTT, and 10 μM zinc sulfate), running at a flow rate of 0.4 mL/min. 50 μL of BSA (30 μM, Thermo Fisher Scientific 23209), or UBQLN1 (514–589, F547Y) at 0.6 or 1.1 mM was injected onto the column. Experiments were performed at 25°C. ASTRA software (version 8.0.2.5) was used for data collection and analyses.

Electrospray ionization mass spectrometry—Mass spectrometry was performed with protein samples (~10 μM) with 10% acetonitrile on a 6100 Series Quadrupole LC mass spectrometer (Agilent Technologies, Inc.), equipped with an electrospray source and operated in the positive ion mode. Data acquisition and analyses were performed using OpenLAB CDS ChemStation Edition C.01.05 (Agilent Technologies, Inc.).

AlphaFold2 prediction—AlphaFold2 was utilized through the computational resources of the High-Performance Computing Biowulf cluster of the NIH (http://hpc.nih.gov). Structures were analyzed and figures generated by using PyMol (PyMOL Molecular Graphics System, http://www.pymol.org) and ChimeraX[77].

K_d fitting—K_d estimates for the UBA and UBAA were performed using the bindfit web server (http://app.supramolecular.org/bindfit/) using the NMR 1:1 preset and the Nelder-Meid fit. Input values were $\Delta\delta_H$ (p.p.m.) values from ^{15}N UBQLN1 (514–589, F547Y) titrated with unlabeled E6AP AZUL. Only residues with $\Delta\delta_H$ values greater than 0.02 p.p.m. were used for the K_d fitting.

QUANTITATION AND STATISTICAL ANALYSIS

Not applicable

Supplementary Material

Refer to Web version on PubMed Central for supplementary material.

Acknowledgements

This work was supported by the Intramural Research Program through the Center for Cancer Research, National Cancer Institute, National Institutes of Health (1ZIABC011627 and the Center for Cancer Research FLEX program to K.J.W.) and in part with federal funds from the National Cancer Institute, National Institutes of Health, under contract 75N91019D00024 (to H.M.). W.M. was supported in part by the NIH Office of Intramural Training and Education's Intramural AIDS Research Fellowship and A.C. was supported by The Intramural Continuing Umbrella of Research Experiences (iCURE) program. This work used computational resources of the High-Performance Computing Biowulf cluster of the NIH (http://hpc.nih.gov). We thank the Optical Microscopy and Image Analysis Lab (OMAL) of NCI-Frederick for training, technical discussions, and use of microscopes. We thank Janusz Koscielniak for maintenance of the NMR spectrometers, and the Biophysics Resource in the Center for Structural Biology, CCR for assistance with LC-MS and CD-spectroscopy. We thank Dr. Angela Gronenborn for suggesting saturation transfer experiments.

Inclusion and Diversity

One or more of the authors of this paper received support from a program designed to increase minority representation in their field of research.

References

1. Chen X, Htet ZM, Lopez-Alfonzo E, Martin A, and Walters KJ (2020). Proteasome interaction with ubiquitinated substrates: from mechanisms to therapies. FEBS J. 10.1111/febs.15638.
2. Osei-Amponsa V, and Walters KJ (2022). Proteasome substrate receptors and their therapeutic potential. Trends Biochem Sci. 10.1016/j.tibs.2022.06.006.
3. Huibregtse JM, Scheffner M, and Howley PM (1993). Cloning and expression of the cDNA for E6-AP, a protein that mediates the interaction of the human papillomavirus E6 oncoprotein with p53. Mol Cell Biol 13, 775–784. 10.1128/mcb.13.2.775-784.1993. [PubMed: 8380895]
4. Huibregtse JM, Scheffner M, and Howley PM (1993). Localization of the E6-AP regions that direct human papillomavirus E6 binding, association with p53, and ubiquitination of associated proteins. Mol Cell Biol 13, 4918–4927. 10.1128/mcb.13.8.4918-4927.1993. [PubMed: 8393140]
5. Scheffner M, Huibregtse JM, Vierstra RD, and Howley PM (1993). The HPV-16 E6 and E6-AP complex functions as a ubiquitin-protein ligase in the ubiquitination of p53. Cell 75, 495–505. 10.1016/0092-8674(93)90384-3. [PubMed: 8221889]
6. Gamell C, Bandilovska I, Gulati T, Kogan A, Lim SC, Kovacevic Z, Takano EA, Timpone C, Agupitan AD, Litchfield C, et al. (2019). E6AP Promotes a Metastatic Phenotype in Prostate Cancer. iScience 22, 1–15. 10.1016/j.isci.2019.10.065. [PubMed: 31739170]
7. Paul PJ, Raghu D, Chan AL, Gulati T, Lambeth L, Takano E, Herold MJ, Hagekyriakou J, Vessella RL, Fedele C, et al. (2016). Restoration of tumor suppression in prostate cancer by targeting the E3 ligase E6AP. Oncogene 35, 6235–6245. 10.1038/onc.2016.159. [PubMed: 27641331]
8. Kishino T, Lalande M, and Wagstaff J (1997). UBE3A/E6-AP mutations cause Angelman syndrome. Nat Genet 15, 70–73. 10.1038/ng0197-70. [PubMed: 8988171]
9. Matsuura T, Sutcliffe JS, Fang P, Galjaard RJ, Jiang YH, Benton CS, Rommens JM, and Beaudet AL (1997). De novo truncating mutations in E6-AP ubiquitin-protein ligase gene (UBE3A) in Angelman syndrome. Nat Genet 15, 74–77. 10.1038/ng0197-74. [PubMed: 8988172]
10. Cooper EM, Hudson AW, Amos J, Wagstaff J, and Howley PM (2004). Biochemical analysis of Angelman syndrome-associated mutations in the E3 ubiquitin ligase E6associated protein. J Biol Chem 279, 41208–41217. 10.1074/jbc.M401302200. [PubMed: 15263005]
11. Samaco RC, Hogart A, and LaSalle JM (2005). Epigenetic overlap in autism-spectrum neurodevelopmental disorders: MECP2 deficiency causes reduced expression of UBE3A and GABRB3. Hum Mol Genet 14, 483–492. 10.1093/hmg/ddi045. [PubMed: 15615769]
12. Lemak A, Yee A, Bezsonova I, Dhe-Paganon S, and Arrowsmith CH (2011). Zn-binding AZUL domain of human ubiquitin protein ligase Ube3A. J Biomol NMR 51, 185–190. 10.1007/s10858-011-9552-y. [PubMed: 21947926]

13. Buel GR, Chen X, Chari R, O'Neill MJ, Ebelle DL, Jenkins C, Sridharan V, Tarasov SG, Tarasova NI, Andresson T, and Walters KJ (2020). Structure of E3 ligase E6AP with a proteasome-binding site provided by substrate receptor hRpn10. Nat Commun 11, 1291. 10.1038/s41467-020-15073-7. [PubMed: 32157086]
14. Miao S, Chen R, Ye J, Tan GH, Li S, Zhang J, Jiang YH, and Xiong ZQ (2013). The Angelman syndrome protein Ube3a is required for polarized dendrite morphogenesis in pyramidal neurons. J Neurosci 33, 327–333. 10.1523/JNEUROSCI.2509-12.2013. [PubMed: 23283345]
15. Avagliano Trezza R, Sonzogni M, Bossuyt SNV, Zampeta FI, Punt AM, van den Berg M, Rotaru DC, Koene LMC, Munshi ST, Stedehouder J, et al. (2019). Loss of nuclear UBE3A causes electrophysiological and behavioral deficits in mice and is associated with Angelman syndrome. Nat Neurosci 22, 1235–1247. 10.1038/s41593-019-0425-0. [PubMed: 31235931]
16. Leggett DS, Hanna J, Borodovsky A, Crosas B, Schmidt M, Baker RT, Walz T, Ploegh H, and Finley D (2002). Multiple associated proteins regulate proteasome structure and function. Mol. Cell 10, 495–507. 10.1016/S1097-2765(02)00638-X. [PubMed: 12408819]
17. Martinez-Noel G, Galligan JT, Sowa ME, Arndt V, Overton TM, Harper JW, and Howley PM (2012). Identification and proteomic analysis of distinct UBE3A/E6AP protein complexes. Mol Cell Biol 32, 3095–3106. 10.1128/MCB.00201-12. [PubMed: 22645313]
18. Wang X, Chen CF, Baker PR, Chen PL, Kaiser P, and Huang L (2007). Mass spectrometric characterization of the affinity-purified human 26S proteasome complex. Biochemistry 46, 3553–3565. 10.1021/bi061994u. [PubMed: 17323924]
19. Besche HC, Sha Z, Kukushkin NV, Peth A, Hock EM, Kim W, Gygi S, Gutierrez JA, Liao H, Dick L, and Goldberg AL (2014). Autoubiquitination of the 26S proteasome on Rpn13 regulates breakdown of ubiquitin conjugates. EMBO J 33, 1159–1176. 10.1002/embj.201386906. [PubMed: 24811749]
20. Yasuda S, Tsuchiya H, Kaiho A, Guo Q, Ikeuchi K, Endo A, Arai N, Ohtake F, Murata S, Inada T, et al. (2020). Stress- and ubiquitylation-dependent phase separation of the proteasome. Nature 578, 296–300. 10.1038/s41586-020-1982-9. [PubMed: 32025036]
21. Uriarte M, Sen Nkwe N, Tremblay R, Ahmed O, Messmer C, Mashtalir N, Barbour H, Masclef L, Voide M, Viallard C, et al. (2021). Starvation-induced proteasome assemblies in the nucleus link amino acid supply to apoptosis. Nat Commun 12, 6984. 10.1038/s41467-021-27306-4. [PubMed: 34848715]
22. Walters KJ, Goh AM, Wang Q, Wagner G, and Howley PM (2004). Ubiquitin family proteins and their relationship to the proteasome: a structural perspective. Biochimica et Biophysica Acta (BBA) - Molecular Cell Research 1695, 73–87. 10.1016/j.bbamcr.2004.10.005. [PubMed: 15571810]
23. Yu C, Yang Y, Wang X, Guan S, Fang L, Liu F, Walters KJ, Kaiser P, and Huang L (2016). Characterization of Dynamic UbR-Proteasome Subcomplexes by In vivo Cross-linking (X) Assisted Bimolecular Tandem Affinity Purification (XBAP) and Label-free Quantitation. Mol Cell Proteomics 15, 2279–2292. 10.1074/mcp.M116.058271. [PubMed: 27114451]
24. Wang X, and Huang L (2008). Identifying dynamic interactors of protein complexes by quantitative mass spectrometry. Mol Cell Proteomics 7, 46–57. 10.1074/mcp.M700261MCP200. [PubMed: 17934176]
25. Collins GA, and Goldberg AL (2020). Proteins containing ubiquitin-like (Ubl) domains not only bind to 26S proteasomes but also induce their activation. Proc Natl Acad Sci U S A 117, 4664–4674. 10.1073/pnas.1915534117. [PubMed: 32071216]
26. Itakura E, Zavodszky E, Shao S, Wohlever ML, Keenan RJ, and Hegde RS (2016). Ubiquilins Chaperone and Triage Mitochondrial Membrane Proteins for Degradation. Mol Cell 63, 21–33. 10.1016/j.molcel.2016.05.020. [PubMed: 27345149]
27. Funakoshi M, Sasaki T, Nishimoto T, and Kobayashi H (2002). Budding yeast Dsk2p is a polyubiquitin-binding protein that can interact with the proteasome. Proc Natl Acad Sci U S A 99, 745–750. 10.1073/pnas.012585199. [PubMed: 11805328]
28. Wilkinson CR, Seeger M, Hartmann-Petersen R, Stone M, Wallace M, Semple C, and Gordon C (2001). Proteins containing the UBA domain are able to bind to multi-ubiquitin chains. Nat Cell Biol 3, 939–943. 10.1038/ncb1001-939. [PubMed: 11584278]

29. Rao H, and Sastry A (2002). Recognition of specific ubiquitin conjugates is important for the proteolytic functions of the ubiquitin-associated domain proteins Dsk2 and Rad23. J Biol Chem 277, 11691–11695. 10.1074/jbc.M200245200. [PubMed: 11805121]
30. Kleijnen MF, Alarcon RM, and Howley PM (2003). The ubiquitin-associated domain of hPLIC-2 interacts with the proteasome. Mol Biol Cell 14, 3868–3875. 10.1091/mbc.e02-11-0766. [PubMed: 12972570]
31. Dao TP, Kolaitis RM, Kim HJ, O'Donovan K, Martyniak B, Colicino E, Hehnly H, Taylor JP, and Castaneda CA (2018). Ubiquitin Modulates Liquid-Liquid Phase Separation of UBQLN2 via Disruption of Multivalent Interactions. Mol Cell 69, 965–978 e966. 10.1016/j.molcel.2018.02.004. [PubMed: 29526694]
32. Zheng T, Galagedera SKK, and Castaneda CA (2021). Previously uncharacterized interactions between the folded and intrinsically disordered domains impart asymmetric effects on UBQLN2 phase separation. Protein Sci 30, 1467–1481. 10.1002/pro.4128. [PubMed: 34029402]
33. Dao TP, Yang Y, Presti MF, Cosgrove MS, Hopkins JB, Ma W, Loh SN, and Castaneda CA (2022). Mechanistic insights into enhancement or inhibition of phase separation by different polyubiquitin chains. EMBO Rep 23, e55056. 10.15252/embr.202255056. [PubMed: 35762418]
34. Walters KJ, Kleijnen MF, Goh AM, Wagner G, and Howley PM (2002). Structural studies of the interaction between ubiquitin family proteins and proteasome subunit S5a. Biochemistry 41, 1767–1777. 10.1021/bi011892y. [PubMed: 11827521]
35. Chen X, Ebelle DL, Wright BJ, Sridharan V, Hooper E, and Walters KJ (2019). Structure of hRpn10 Bound to UBQLN2 UBL Illustrates Basis for Complementarity between Shuttle Factors and Substrates at the Proteasome. J Mol Biol 431, 939–955. 10.1016/j.jmb.2019.01.021. [PubMed: 30664872]
36. Alexander EJ, Ghanbari Niaki A, Zhang T, Sarkar J, Liu Y, Nirujogi RS, Pandey A, Myong S, and Wang J (2018). Ubiquilin 2 modulates ALS/FTD-linked FUS-RNA complex dynamics and stress granule formation. Proc Natl Acad Sci U S A 115, E11485–E11494. 10.1073/pnas.1811997115. [PubMed: 30442662]
37. Gerson JE, Linton H, Xing J, Sutter AB, Kakos FS, Ryou J, Liggans N, Sharkey LM, Safren N, Paulson HL, and Ivanova MI (2021). Shared and divergent phase separation and aggregation properties of brain-expressed ubiquilins. Sci Rep 11, 287. 10.1038/s41598-020-78775-4. [PubMed: 33431932]
38. Kuhnle S, Martinez-Noel G, Leclere F, Hayes SD, Harper JW, and Howley PM (2018). Angelman syndrome-associated point mutations in the Zn(2+)-binding N-terminal (AZUL) domain of UBE3A ubiquitin ligase inhibit binding to the proteasome. J Biol Chem 293, 18387–18399. 10.1074/jbc.RA118.004653. [PubMed: 30257870]
39. Burke KA, Janke AM, Rhine CL, and Fawzi NL (2015). Residue-by-Residue View of In Vitro FUS Granules that Bind the C-Terminal Domain of RNA Polymerase II. Mol Cell 60, 231–241. 10.1016/j.molcel.2015.09.006. [PubMed: 26455390]
40. Zacharias DA, Violin JD, Newton AC, and Tsien RY (2002). Partitioning of lipid-modified monomeric GFPs into membrane microdomains of live cells. Science 296, 913916. 10.1126/science.1068539.
41. Zhang D, Raasi S, and Fushman D (2008). Affinity makes the difference: nonselective interaction of the UBA domain of Ubiquilin-1 with monomeric ubiquitin and polyubiquitin chains. J Mol Biol 377, 162–180. 10.1016/j.jmb.2007.12.029. [PubMed: 18241885]
42. Jumper J, Evans R, Pritzel A, Green T, Figurnov M, Ronneberger O, Tunyasuvunakool K, Bates R, Zidek A, Potapenko A, et al. (2021). Highly accurate protein structure prediction with AlphaFold. Nature 596, 583–589. 10.1038/s41586-021-03819-2. [PubMed: 34265844]
43. Tunyasuvunakool K, Adler J, Wu Z, Green T, Zielinski M, Zidek A, Bridgland A, Cowie A, Meyer C, Laydon A, et al. (2021). Highly accurate protein structure prediction for the human proteome. Nature 596, 590–596. 10.1038/s41586-021-03828-1. [PubMed: 34293799]
44. Shen Y, Delaglio F, Cornilescu G, and Bax A (2009). TALOS+: a hybrid method for predicting protein backbone torsion angles from NMR chemical shifts. J Biomol NMR 44, 213–223. 10.1007/s10858-009-9333-z. [PubMed: 19548092]

45. van Dieck J (2018). Stoichiometry of Intrinsically-Disordered Protein Complexes. Application note AN1610.

46. Evans R, O'Neill M, Pritzel A, Antropova N, Senior A, Green T, Žídek A, Bates R, Blackwell S, Yim J, et al. (2022). Protein complex prediction with AlphaFold-Multimer. bioRxiv, 2021.2010.2004.463034. 10.1101/2021.10.04.463034.

47. Kleijnen MF, Shih AH, Zhou P, Kumar S, Soccio RE, Kedersha NL, Gill G, and Howley PM (2000). The hPLIC proteins may provide a link between the ubiquitination machinery and the proteasome. Mol Cell 6, 409–419. 10.1016/s1097-2765(00)00040-x. [PubMed: 10983987]

48. Thordarson P (2011). Determining association constants from titration experiments in supramolecular chemistry. Chem Soc Rev 40, 1305–1323. 10.1039/c0cs00062k. [PubMed: 21125111]

49. Walters KJ, Matsuo H, and Wagner G (1997). A simple method to distinguish intermonomer nuclear overhauser effects in homodimeric proteins with C-2 symmetry. J Am Chem Soc 119, 5958–5959. DOI 10.1021/ja963309k.

50. Schwieters CD, Kuszewski JJ, Tjandra N, and Clore GM (2003). The Xplor-NIH NMR molecular structure determination package. J Magn Reson 160, 65–73. 10.1016/s1090-7807(02)00014-9. [PubMed: 12565051]

51. Buel GR, and Walters KJ (2022). Can AlphaFold2 predict the impact of missense mutations on structure? Nat Struct Mol Biol 29, 1–2. 10.1038/s41594-021-00714-2. [PubMed: 35046575]

52. Barbarin-Bocahu I, and Graille M (2022). The X-ray crystallography phase problem solved thanks to AlphaFold and RoseTTAFold models: a case-study report. Acta Crystallogr D 78, 517–531. 10.1107/S2059798322002157.

53. Flower TG, and Hurley JH (2021). Crystallographic molecular replacement using an in silico-generated search model of SARS-CoV-2 ORF8. Protein Science 30, 728–734. 10.1002/pro.4050. [PubMed: 33625752]

54. Ferrario E, Miggiano R, Rizzi M, and Ferraris DM (2022). The integration of AlphaFold-predicted and crystal structures of human trans-3-hydroxy-l-proline dehydratase reveals a regulatory catalytic mechanism. Comput Struct Biotechnol J 20, 3874–3883. 10.1016/j.csbj.2022.07.027. [PubMed: 35891782]

55. McCoy AJ, Sammito MD, and Read RJ (2022). Implications of AlphaFold2 for crystallographic phasing by molecular replacement. Acta Crystallogr D Struct Biol 78, 1–13. 10.1107/S2059798321012122. [PubMed: 34981757]

56. Cramer P (2021). AlphaFold2 and the future of structural biology. Nat Struct Mol Biol 28, 704–705. 10.1038/s41594-021-00650-1. [PubMed: 34376855]

57. Peeples W, and Rosen MK (2021). Mechanistic dissection of increased enzymatic rate in a phase-separated compartment. Nat Chem Biol 17, 693–702. 10.1038/s41589-021-00801-x. [PubMed: 34035521]

58. Wu X, Ganzella M, Zhou J, Zhu S, Jahn R, and Zhang M (2021). Vesicle Tethering on the Surface of Phase-Separated Active Zone Condensates. Mol Cell 81, 13–24 e17. 10.1016/j.molcel.2020.10.029. [PubMed: 33202250]

59. Milovanovic D, Wu Y, Bian X, and De Camilli P (2018). A liquid phase of synapsin and lipid vesicles. Science 361, 604–607. 10.1126/science.aat5671. [PubMed: 29976799]

60. Osei-Amponsa V, and Walters KJ (2022). Proteasome substrate receptors and their therapeutic potential. Trends Biochem Sci 47, 950–964. 10.1016/j.tibs.2022.06.006. [PubMed: 35817651]

61. Husnjak K, Elsasser S, Zhang N, Chen X, Randles L, Shi Y, Hofmann K, Walters KJ, Finley D, and Dikic I (2008). Proteasome subunit Rpn13 is a novel ubiquitin receptor. Nature 453, 481–488. 10.1038/nature06926. [PubMed: 18497817]

62. Chen X, Randles L, Shi K, Tarasov SG, Aihara H, and Walters KJ (2016). Structures of Rpn1 T1:Rad23 and hRpn13:hPLIC2 Reveal Distinct Binding Mechanisms between Substrate Receptors and Shuttle Factors of the Proteasome. Structure 24, 1257–1270. 10.1016/j.str.2016.05.018. [PubMed: 27396824]

63. Delaglio F, Grzesiek S, Vuister GW, Zhu G, Pfeifer J, and Bax A (1995). NMRPipe: a multidimensional spectral processing system based on UNIX pipes. J Biomol NMR 6, 277–293. 10.1007/BF00197809. [PubMed: 8520220]

64. Bartels C, Xia TH, Billeter M, Guntert P, and Wuthrich K (1995). The program XEASY for computer-supported NMR spectral analysis of biological macromolecules. J Biomol NMR 6, 1–10. 10.1007/BF00417486. [PubMed: 22911575]

65. Lee W, Tonelli M, and Markley JL (2015). NMRFAM-SPARKY: enhanced software for biomolecular NMR spectroscopy. Bioinformatics 31, 1325–1327. 10.1093/bioinformatics/btu830. [PubMed: 25505092]

66. Peng JW, G. (1994). Protein Mobility from multiple 15N Relaxation Parameters.

67. Ishima R, and Torchia DA (2006). Accuracy of optimized chemical-exchange parameters derived by fitting CPMG R2 dispersion profiles when R2(0a) not = R2(0b). J Biomol NMR 34, 209–219. 10.1007/s10858-005-6226-7. [PubMed: 16645811]

68. Carver JP, and Richards RE (1972). General 2-Site Solution for Chemical Exchange Produced Dependence of T2 Upon Carr-Purcell Pulse Separation. J Magn Reson 6, 89–&. Doi 10.1016/0022-2364(72)90090-X.

69. Jen J (1978). Chemical Exchange and Nmr T2 Relaxation - Multisite Case. J Magn Reson 30, 111–128. Doi 10.1016/0022-2364(78)90229-9.

70. Davis DG, Perlman ME, and London RE (1994). Direct measurements of the dissociation-rate constant for inhibitor-enzyme complexes via the T1 rho and T2 (CPMG) methods. J Magn Reson B 104, 266–275. 10.1006/jmrb.1994.1084. [PubMed: 8069484]

71. Korzhnev DM, Salvatella X, Vendruscolo M, Di Nardo AA, Davidson AR, Dobson CM, and Kay LE (2004). Low-populated folding intermediates of Fyn SH3 characterized by relaxation dispersion NMR. Nature 430, 586–590. 10.1038/nature02655. [PubMed: 15282609]

72. Schindelin J, Arganda-Carreras I, Frise E, Kaynig V, Longair M, Pietzsch T, Preibisch S, Rueden C, Saalfeld S, Schmid B, et al. (2012). Fiji: an open-source platform for biological-image analysis. Nat Methods 9, 676–682. 10.1038/nmeth.2019. [PubMed: 22743772]

73. Provencher SW, and Glockner J (1981). Estimation of globular protein secondary structure from circular dichroism. Biochemistry 20, 33–37. 10.1021/bi00504a006. [PubMed: 7470476]

74. van Stokkum IH, Spoelder HJ, Bloemendal M, van Grondelle R, and Groen FC (1990). Estimation of protein secondary structure and error analysis from circular dichroism spectra. Anal Biochem 191, 110–118. 10.1016/0003-2697(90)90396-q. [PubMed: 2077933]

75. Miles AJ, Ramalli SG, and Wallace BA (2022). DichroWeb, a website for calculating protein secondary structure from circular dichroism spectroscopic data. Protein Sci 31, 37–46. 10.1002/pro.4153. [PubMed: 34216059]

76. Lees JG, Miles AJ, Wien F, and Wallace BA (2006). A reference database for circular dichroism spectroscopy covering fold and secondary structure space. Bioinformatics 22, 1955–1962. 10.1093/bioinformatics/btl327. [PubMed: 16787970]

77. Pettersen EF, Goddard TD, Huang CC, Meng EC, Couch GS, Croll TI, Morris JH, and Ferrin TE (2021). UCSF ChimeraX: Structure visualization for researchers, educators, and developers. Protein Sci 30, 70–82. 10.1002/pro.3943. [PubMed: 32881101]

Highlights

- Discovery of E6AP AZUL interaction with UBQLN1/2 UBA domain
- E6AP AZUL associates with UBQLN2 biomolecular condensates
- E6AP AZUL:UBQLN1 UBA structure by merging NOE data with AlphaFold2-Multimer
- UBA-adjacent helix self-associates and allosterically senses AZUL:UBA binding

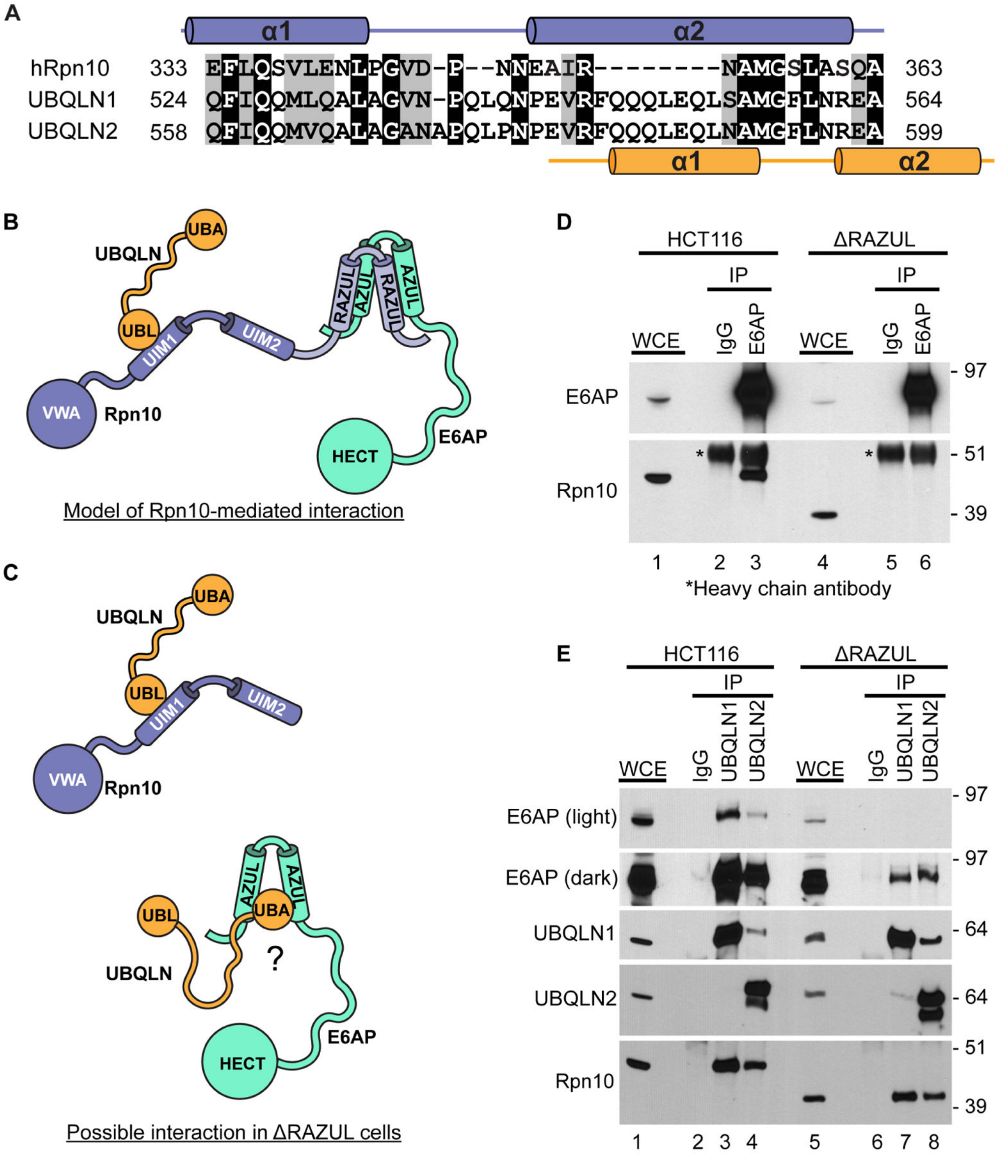

Figure 1. UBQLN1 and UBQLN2 interact with E6AP in cells.

A) BLAST search results from uniprot.org using UniProtKB reference proteomes and Swiss-Prot databases showing sequence similarity between hRpn10 E333-A363 and a region near the C-terminus of UBQLN1 and UBQLN2. See also Figure S1 for UBQLN family sequence alignment. B) Model illustrating known interactions that may provide a means for E6AP and UBQLN1/2 to interact indirectly through hRpn10. C) Model illustrating how E6AP interaction with hRpn10 is lost in ΔRAZUL cells, where UBQLN1/2 interactions with hRpn10 are expected to be preserved. D) HCT116 or ΔRAZUL cells were subjected to crosslinking with DSP followed by immunoprecipitation with anti-E6AP or control antibodies. Whole cell extracts (WCE) and E6AP-immunoprecipitates were immunoblotted with the indicated antibodies. Note that hRpn10 co-precipitates with E6AP in HCT116 cells, but this interaction is lost in ΔRAZUL cells. E) HCT116 or ΔRAZUL cells were subjected to crosslinking with DSP followed by immunoprecipitation with anti-

UBQLN1, anti-UBQLN2, or control antibodies. WCE and UBQLN-immunoprecipitates were immunoblotted with the indicated antibodies. E6AP is observed in both anti-UBQLN1 and anti-UBQLN2 co-precipitates in ΔRAZUL cells, albeit at lower amounts than in HCT116 cells.

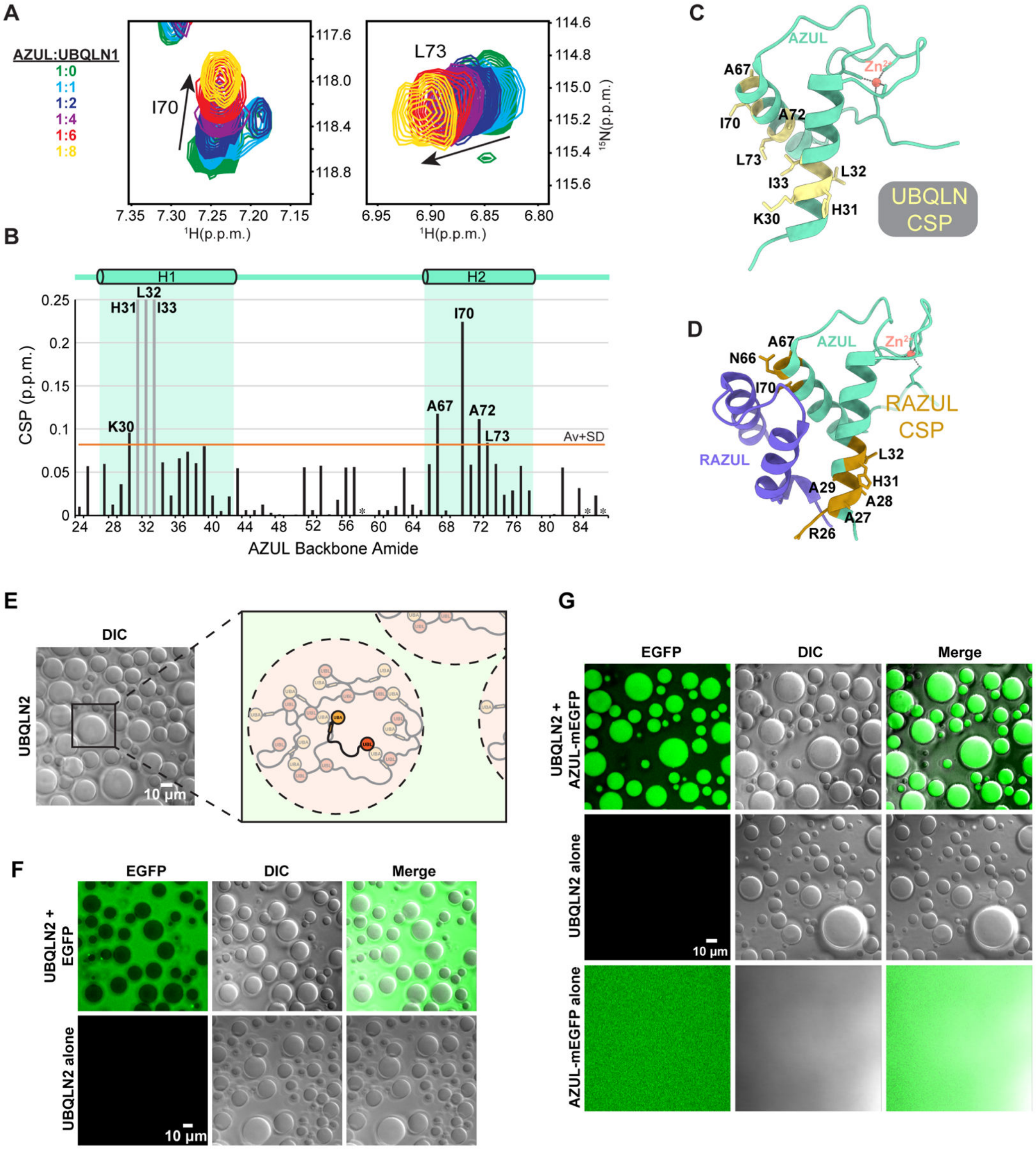

Figure 2. E6AP AZUL binds to the UBQLN1 C-terminal region and is recruited to UBQLN2 condensates *in vitro*.

A) Overlays of the amide signals for AZUL I70 and L73 at varying molar ratios with UBQLN1. See Figure S2 for full spectrum. B) Chemical shift perturbation (CSP) values derived from (A) plotted according to AZUL residue number. Gray bars indicate residues whose peaks disappeared following addition of UBQLN1. The value corresponding to one standard deviation above the mean is indicated with an orange line. C) Ribbon diagram of E6AP AZUL in which residues with CSPs over one standard deviation above the mean or having disappeared after addition of UBQLN1 are shown in yellow with side chains represented as sticks. D) Ribbon diagram of AZUL binding to the hRpn10 RAZUL (PDB 6u19) with RAZUL shown in slate blue and residues with CSPs following RAZUL addition shown in gold. E) DIC microscopy image showing 50 μM UBQLN2 in 20 mM $NaPO_4$, 200 mM NaCl, and 2.5 μM $ZnSO_4$ (pH 6.8) forming biomolecular condensates at 37 °C. Diagram to the right illustrates the high-density state thought to exist in UBQLN2 condensates, mediated by a large number of weak interactions between UBQLN2 monomers. F) Control experiment with UBQLN2 in the same conditions as (A) (bottom panels), or additionally containing 25 μM EGFP (top panels). Note that UBQLN2 does not fluoresce on its own (bottom left panel), and that EGFP does not colocalize with the condensates. G) 50 μM UBQLN2 and 25 μM AZUL-mEGFP in 20 mM $NaPO_4$, 200 mM NaCl, and 2.5 μM $ZnSO_4$ (pH 6.8) at 37 °C (top panels) or without AZUL-mEGFP (middle panels) or without UBQLN2 (bottom panels). AZUL-mEGFP alone does form condensates (bottom panels), nor does UBQLN2 fluoresce on its own (middle panels). When mixed together, AZUL-mEGFP preferentially localizes to UBQLN2 condensates (top panels).

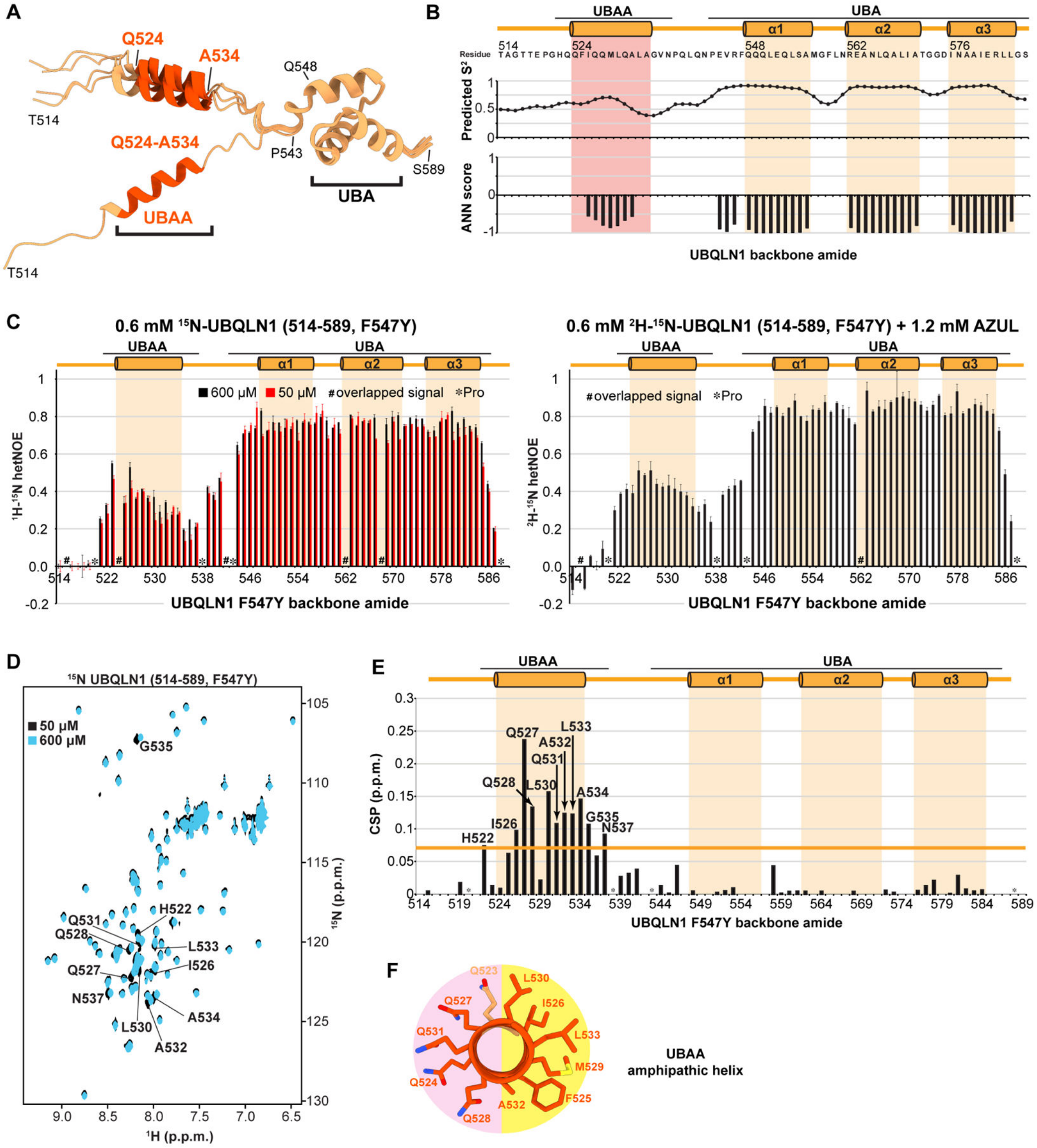

Figure 3. A UBA adjacent region forms a distinct, helical domain that appears to self-associate.

A) AlphaFold2-predicted structures of UBQLN1 514–589 aligned based on the UBA domain. Residues predicted to be helical from data shown in (B and Fig S3A) are depicted in orange. B) TALOS+ prediction of UBQLN1 (514–586) secondary structure, with predicted order parameters S^2 in the middle panel, and negative values in the bottom panel indicating alpha-helical prediction. Data was collected on a 0.35 mM sample. See also Figure S3A for NOESY data in support of UBAA helicity. C) ^1H-^{15}N hetNOE values for UBQLN1 (514–589, F547Y) (left) and ^2H-^{15}N hetNOE values for UBQLN1 (514–589, F547Y) mixed with AZUL at a 1:2 ratio (right). D) ^{15}N-HSQC spectra of ^{15}N-UBQLN1 (514–589, F547Y) at 50 μM (black) and 600 μM (blue). Peaks that shift over one standard deviation above the mean are labeled. E) CSPs derived from (A) are plotted according to UBQLN1 (F547Y) residue number. The value corresponding to one standard deviation above the mean is indicated with an orange line. See also Figure S3B for circular dichroism data of UBQLN1 with and without AZUL. F) Lengthwise view of the UBAA illustrating the amphipathy of the helix, with coloring as in (A).

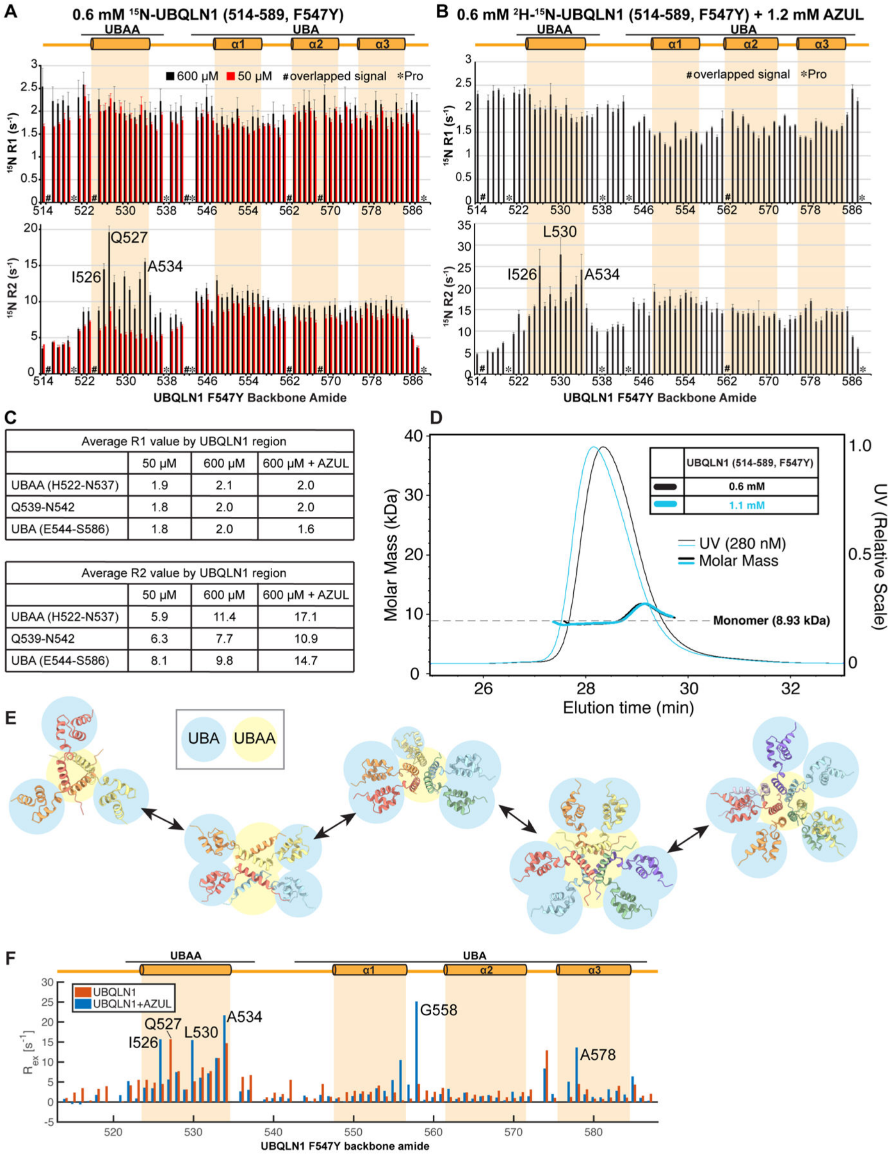

Average R1 value by UBQLN1 region			
	50 μM	600 μM	600 μM + AZUL
UBAA (H522-N537)	1.9	2.1	2.0
Q539-N542	1.8	2.0	2.0
UBA (E544-S586)	1.8	2.0	1.6

Average R2 value by UBQLN1 region			
	50 μM	600 μM	600 μM + AZUL
UBAA (H522-N537)	5.9	11.4	17.1
Q539-N542	6.3	7.7	10.9
UBA (E544-S586)	8.1	9.8	14.7

Figure 4. The UBQLN1 UBAA helix undergoes dynamic exchange and is more ordered at higher concentrations.

A-B) ^{15}N R_1 (longitudinal) relaxation rates and ^{15}N R_2 (transverse) relaxation rates for A) ^{1}H-^{15}N-UBQLN1 (514–589, F547Y) or B) ^{2}H-^{15}N-UBQLN1 (514–589, F547Y) mixed with unlabeled AZUL at a 1:2 ratio. C) Average R_1 and R_2 values for UBQLN1 regions. D) SEC-MALS traces for UBQLN1 (514–589, F547Y) at 0.6 and 1.1 mM. E) AlphaFold2-Multimer predicted structures of UBQLN1 (514–589) for oligomeric states ranging from trimer to heptamer. The UBA domain of each UBQLN1 monomer is highlighted in blue, UBAA domain is highlighted in yellow. In all cases, the UBAA is predicted to cluster in the center with the UBA pointed out. F) R_{ex} values from CPMG R_2 relaxation dispersion collected at 850 MHz with and without AZUL. See also Figure S4 for R_{ex} values collected at 850 and 600 MHz with and without AZUL.

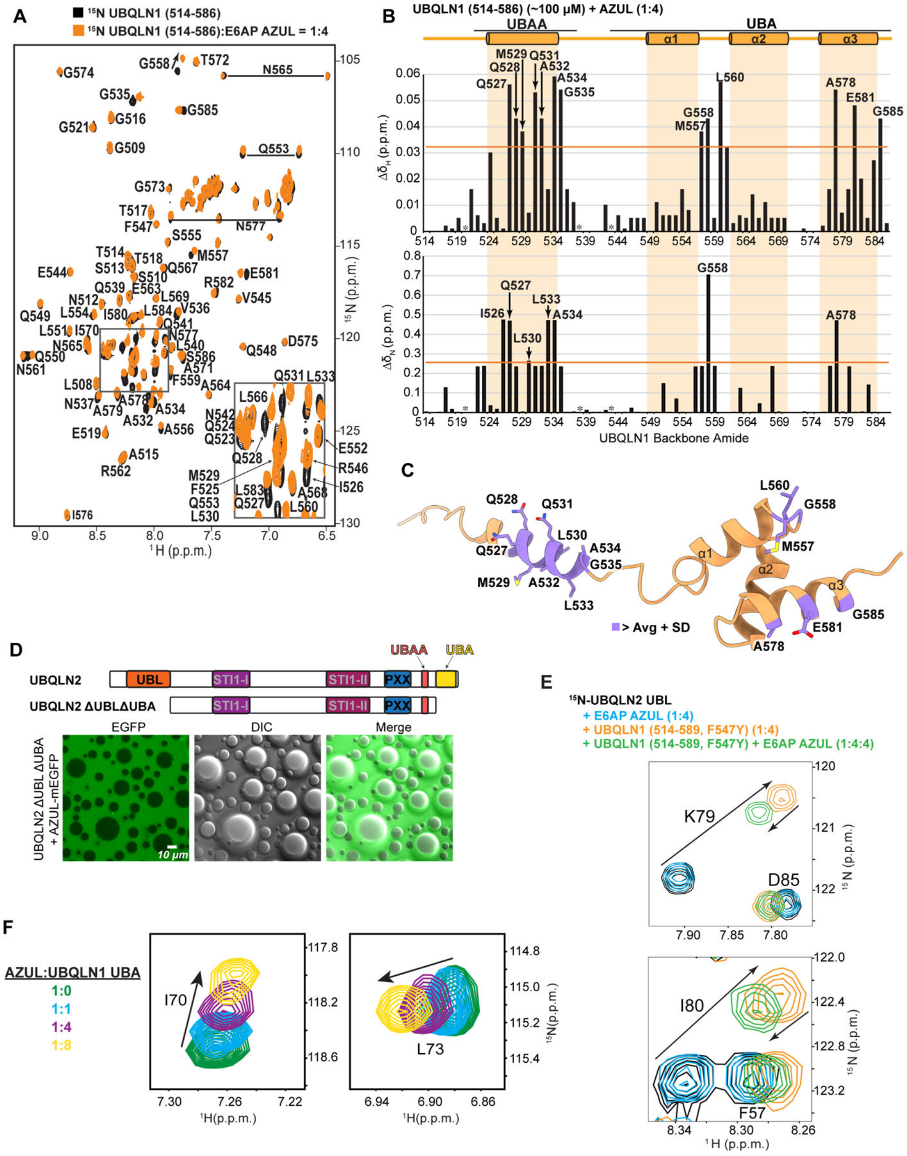

Figure 5. E6AP AZUL binds UBQLN UBA.

A) ^{15}N-HSQC spectra of ^{15}N-UBQLN1 (514–586) at approximately 100 μM (black) overlayed with that of ^{15}N-UBQLN1 (514–586) mixed with 400 μM unlabeled E6AP AZUL (orange). B) Changes in hydrogen (top) or nitrogen (bottom) chemical shift values derived from (A) are plotted according to UBQLN1 residue. C) Residues with chemical shift changes one standard deviation above the mean (orange line) are shown in purple on the AlphaFold2-predicted structure of UBQLN1 514–589. D) Schematic of UBQLN2 domains and truncation construct (top). Lower panels show 50 μM UBQLN2 ΔUBLΔUBA and 25 μM AZUL-mEGFP in 20 mM $NaPO_4$, 200 mM NaCl, and 2.5 μM $ZnSO_4$ (pH 6.8) at 37 °C. AZUL-mEGFP is excluded from UBQLN2 ΔUBLΔUBA condensates. E) Zoomed views of ^{15}N-HSQC spectra comparing ^{15}N-UBQLN2 UBL (black) or with 4-fold molar excess unlabeled AZUL (blue), UBQLN1 (514–589, F547Y) (orange), or both AZUL and UBQLN1 (514–589, F547Y) (green). See also Figure S5B for K_d fitting from CSPs from a replicate titration. F) Overlays of AZUL I70 and L73 amide peaks from ^{15}N-AZUL titrated with UBQLN1 UBA (541–589). See also Figure S5C for the full spectra.

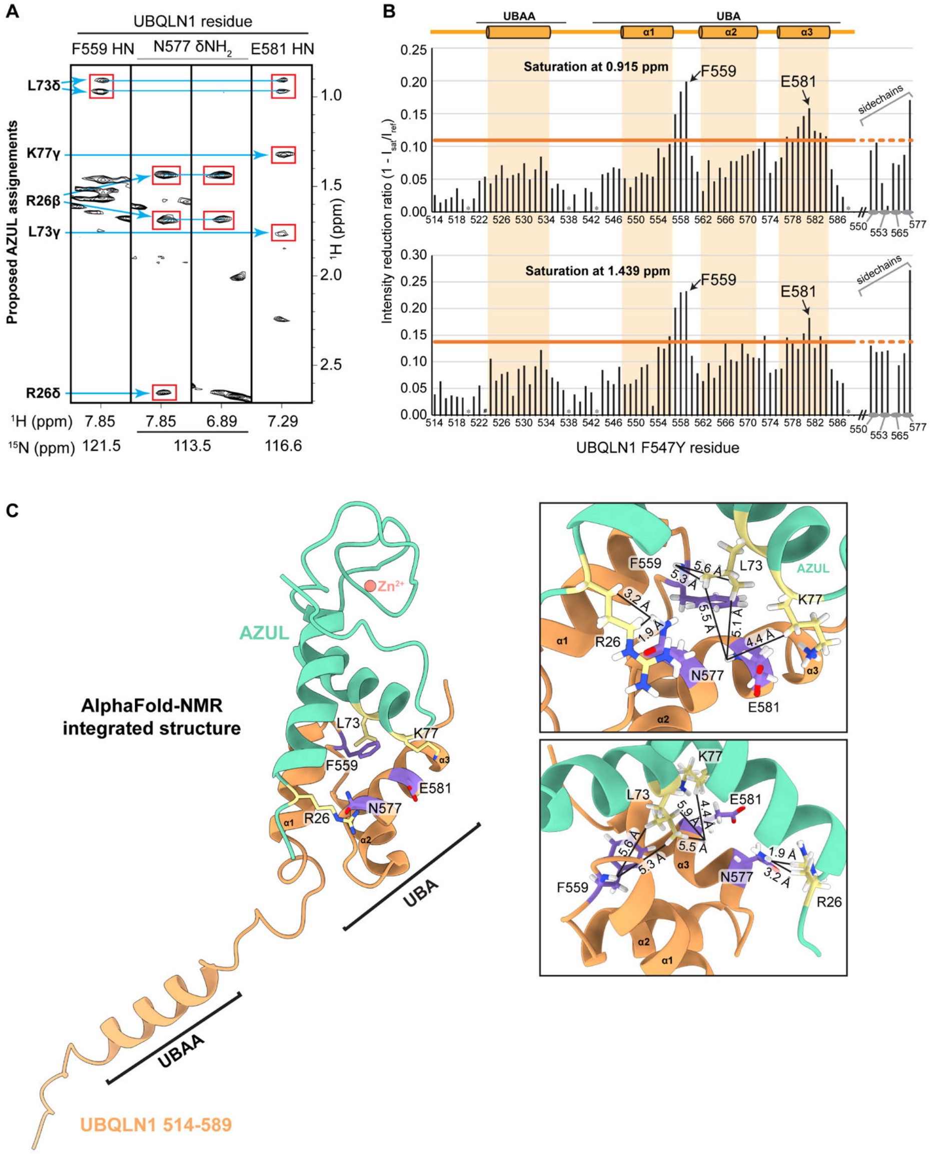

Figure 6. A structural model for E6AP AZUL binding to UBQLN1 UBA based on AlphaFold2-Multimer and NMR NOESY data.

A) Selected regions of a ^{15}N-edited NOESY collected on 0.6 mM ^{2}H-^{15}N UBQLN1 (514–589, F547Y) mixed with 1.2 mM unlabeled AZUL. Assignments from AZUL residues are indicated with red boxes. B) Intensity reduction ratios following saturation at 0.915 (top) or 1.439 (bottom) with the same sample as in (A). See also Figure S6 for labeling scheme used in (A-B) and intramolecular NOEs detected. C) AlphaFold2-NMR integrated structure in which NOE assignments from AZUL were assigned guided by the AlphaFold2-Multimer-predicted structure and inputted as distance constraints into Xplor-NIH. Insets (right) show expanded regions to highlight distances between protons with assigned intermolecular NOEs. Residues from UBQLN1 with NOEs detected to their amides are shown in purple; residues from AZUL with assigned NOEs are shown in yellow; side chain nitrogen and oxygen atoms are in blue and red respectively. See also Figure S7A for initial AlphaFold predicted structure generated prior to the AlphaFold-NMR integrated structure. See Figure

S7B for overlay of the initial AlphaFold structure with the AlphaFold-NMR integrated structure.

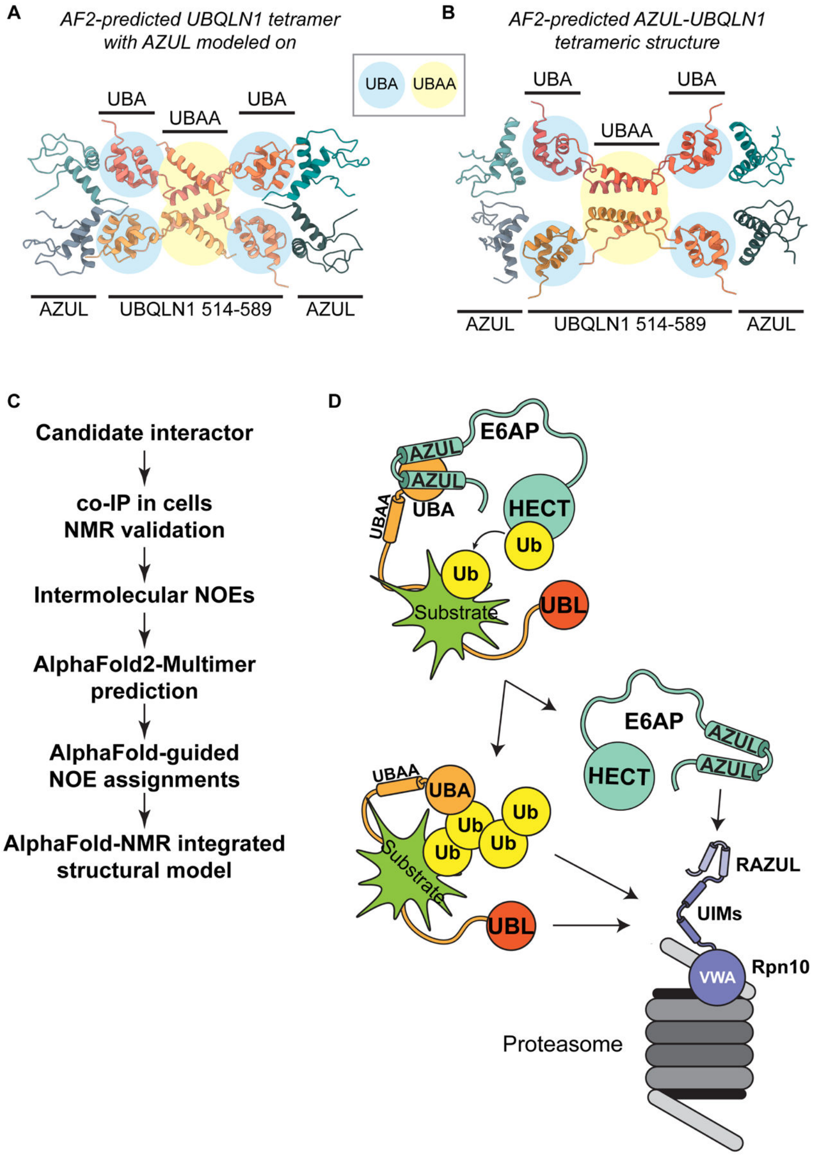

Figure 7. Comprehensive model and workflow of the E6AP AZUL:UBQLN1 interaction.

A) AlphaFold2-Multimer model of a UBQLN1 (514–589) tetramer (orange and red) as in Fig 4E, with AZUL (blue) modeled on based on the AlphaFold-NMR integrated structure. B) AlphaFold2-Multimer model of four UBQLN1 (514–589) and four AZUL molecules. C) Workflow developed in the current study to use NMR and AlphaFold iteratively. D) Depiction of how E6AP may interact with UBQLN1/2 UBA, highlighting the proximity this would afford E6AP to UBQLN1/2-bound substrates, presumably allowing for E6AP-mediated ubiquitination of UBQLN1/2-bound substrates. Following ubiquitination, it is expected that the UBA domain would bind to substrate-attached ubiquitin chain(s), displacing the E6AP AZUL from the UBA. The ubiquitinated substrate: UBQLN complex could then bind to proteasome substrate receptors either through the substrate-attached ubiquitin chain or the UBL domain of UBQLN1/2.

Key resources table

REAGENT or RESOURCE	SOURCE	IDENTIFIER
Antibodies		
Mouse monoclonal anti-E6AP (immunoblot)	Sigma-Aldrich	Cat# E8655; RRID:AB_261956
Rabbit polyclonal anti-E6AP (Immunoprecipitation)	ProteinTech	Cat# 10344–1-AP; RRID:AB_2211801
Mouse monoclonal anti-UBQLN2 (immunoblot)	Novus Biologicals	Cat# NBP2–25164; RRID:AB_2885154
Rabbit monoclonal anti-UBQLN2 (immunoprecipitation)	Cell Signaling Technology	Cat# 85509; RRID:AB_2800056
Rabbit monoclonal anti-UBQLN1	Cell Signaling Technology	Cat# 14526; RRID:AB_2798502
Rabbit monoclonal anti-hRpn10/PSMD4	Cell Signaling Technology	Cat# 3336; RRID:AB_11178520
Rabbit polycolonal IgG control (immunoprecipitation)	Sigma-Aldrich	Cat# 12–370
Goat polyclonal anti-mouse IgG (Fab specific), peroxidase conjugated	Sigma-Aldrich	Cat# A9917; RRID:AB_258476
Mouse monoclonal anti-rabbit IgG (native specific), peroxidase conjugated	Sigma-Aldrich	Cat# R3155; RRID:AB_1079117
Bacterial and virus strains		
Escherichia coli DH5α competent cells	Invitrogen	Cat# 18265017
Escherichia coli BL21(DE3) competent cells	Invitrogen	Cat# C600003
Chemicals, peptides, and recombinant proteins		
^{15}N Ammonium Chloride	Cambridge Isotope Laboratories, Inc.	Cat# NLM-467–1
^{13}C Glucose	Cambridge Isotope Laboratories, Inc.	Cat# CLM-1396-PK
D_2O	Cambridge Isotope Laboratories, Inc.	Cat# DLM-4-99-1000
BioExpress cell growth media	Cambridge Isotope Laboratories, Inc.	CGM-1000-DN
PreScission Protease	Cytiva	Cat# 27084301
Protease inhibitor cocktail	Roche	11836153001
EDTA-free Protease inhibitor cocktail	Roche	11836170001
Glutathione S-sepharose 4B	Cytiva	Cat# 17075605
Ni-NTA agarose resin	Qiagen	Cat# 30210
Protein A Dynabeads	Invitrogen	Cat# 10002D
Enhanced Green Fluorescent Protein (EGFP)	Chromotek	Cat# EGFP-250
UBQLN1	This paper	N/A
UBQLN1 (514–586)	This paper	N/A
UBQLN1 (514–589, F547Y)	This paper	N/A
UBQLN1 UBA (541–589)	This paper	N/A
UBQLN2	This paper	N/A
UBQLN2 ΔUBLΔUBA (109–576)	This paper	N/A
UBQLN2 UBL (26–103)	This paper	N/A
E6AP AZUL (Isoform II 24–87)	This paper	N/A
AZUL-mEGFP (E6AP isoform II 24–87 with a C-terminal mEGFP)	This paper	N/A

REAGENT or RESOURCE	**SOURCE**	**IDENTIFIER**
Deposited data		
NMR structure of E6AP AZUL	Protein Data Bank ref. Lemak et al.[12]	PDB: 2KR1
Chemical shift data for E6AP AZUL	BMRB ref. Lemak et al.[12]	BMRB: 16620
NMR structure of E6AP AZUL in complex with hRpn10 RAZUL	Protein Data Bank ref. Buel et al.[13]	PDB: 6U19
Chemical shift data for E6AP AZUL in complex with hRpn10 RAZUL	BMRB ref. Buel et al.[13]	BMRB: 27875
NMR structure of UBQLN1 UBA	Protein Data Bank ref. Zhang et al.[41]	PDB: 2JY5
Chemical shift data for UBQLN1 514–586	This paper	BMRB: 51768
Chemical shift data for UBQLN1 514–589, F547Y at 50 μM	This paper	BMRB: 51769
Chemical shift data for UBQLN1 514–589, F547Y at 600 μM	This paper	BMRB: 51770
Experimental models: Cell lines		
Human: HCT116 cells	ATCC	CCL-247
Human: ΔRAZUL clone 13	Ref. Buel et al.[13]	N/A
Recombinant DNA		
pGEX-6P-1-UBQLN1	Genscript (this paper)	N/A
pGEX-6P-3-UBQLN1 (514–586)	Genscript (this paper)	N/A
pGEX-6P-3-UBQLN1 (514–589, F547Y)	Genscript (this paper)	N/A
pGEX-6P-1-UBQLN1 UBA (541–589)	Genscript (this paper)	N/A
pGEX-6P-1-UBQLN2	Genscript (this paper)	N/A
pGEX-6P-1-mCherry-UBQLN2 ΔUBLΔUBA (109–576)	Genscript (this paper)	N/A
pGEX-2T-UBQLN2 UBL (26–103)	Refs. Chen et al.[35,62]	N/A
pET28a-E6AP AZUL (Isoform II 24–87)	Ref. Buel et al.[13]	N/A
pGEX-6P-1-AZUL-mEGFP (E6AP isoform II 24–87 with a C-terminal mEGFP)	Genscript (this paper)	N/A
Software and algorithms		
AlphaFold2	Ref. Jumper et al.[42]	N/A
XPLOR-NIH	Ref. Schwieters et al.[50]	https://nmr.cit.nih.gov/xplor-nih/
XEASY	Ref. Bartels et al.[64]	N/A
NMRPipe	Ref. Delaglio et al.[63]	https://www.ibbr.umd.edu/nmrpipe/install.html
TALOS+	Ref. Shen et al.[44]	https://spin.niddk.nih.gov/bax/software/TALOS/
PyMOL	Schrodinger	http://www.pymol.org
ChimeraX	Ref. Pettersen et al.[77]	https://www.rbvi.ucsf.edu/chimerax/
Fiji	Ref. Schindelin et al.[72]	https://imagej.net/software/fiji/